

# Modelling the delayed shock-breakout emission following jet-launching binary neutron star mergers via relativistic MHD simulations

Matteo Pais<sup>1,2\*</sup>, Riccardo Ciolfi<sup>1,2</sup>, and Andrea Pavan<sup>1,2</sup>

<sup>1</sup> INAF, Osservatorio Astronomico di Padova, Vicolo dell'Osservatorio 5, I-35122, Padova, Italy

<sup>2</sup> INFN, Sezione di Padova, Via Francesco Marzolo 8, I-35131 Padova, Italy

Received DDMM, 2026

## ABSTRACT

*Context.* In binary neutron star (BNS) mergers launching a relativistic jet, an electromagnetic (EM) signal is produced when the jet-driven shock breaks out of the merger ejecta. The observed time delay of this shock-breakout (SBO) emission with respect to the gravitational-wave (GW) signal from the merger provides a powerful probe of the physical conditions governing jet launching and early-time jet propagation.

*Aims.* Considering different models of jet propagation in realistic post-merger environments, we investigate the SBO emission and corresponding GW-EM delay that would be observed depending on the viewing angle and the assumed ejecta opacity.

*Methods.* We perform relativistic magneto-hydrodynamic simulations of jets propagating through a post-merger environment directly imported from the outcome of a previous BNS merger simulation. We also introduce a specific procedure to faithfully reconstruct the early dynamical ejecta up to their natural front. The evolution is followed in 3D up to 0.6 s and then continued imposing axisymmetry and 8 times higher resolution. Varying jet launching time and luminosity, we identify three representative models spanning regimes from early breakout to extended jet choking. For each case, we track the jet-driven forward shock up to the photosphere and compute the angle-dependent bolometric SBO luminosity, assuming full conversion of the thermal energy within the shocked material into radiation, and taking into account non-radial photon propagation, relativistic Doppler shifts, and light-travel-time effects. We consider two opacity values spanning a factor of 10.

*Results.* We find that the GW-EM delay depends only weakly on both the viewing angle and the ejecta opacity, making it a robust diagnostic for constraining models. Comparing our three models with GRB 170817A, the one resulting in a substantially choked jet provides the most plausible peak bolometric luminosity and the closest match to the observed GW-EM delay and signal duration.

**Key words.** Stars: neutron – Stars: jets – Gamma-ray burst: general – Magnetohydrodynamics (MHD) – Methods: numerical – Relativistic processes

## 1. Introduction

The detection of gravitational waves (GWs) and electromagnetic (EM) emission from the binary neutron star (BNS) merger GW170817 marked the beginning of multi-messenger astrophysics with GW sources (Abbott et al. 2017a,b,c). The EM counterparts of the event included a short gamma-ray burst (GRB) and a kilonova, the latter being powered by the radioactive decay of heavy elements synthesized in the merger ejecta (Metzger 2020). Together, these observations offer a unique opportunity to probe the physics of compact binary mergers, relativistic outflows, and  $r$ -process nucleosynthesis.

The prompt gamma-ray signal accompanying the event, named GRB 170817A, resulted orders of magnitude less luminous than typical short GRBs, leaving initial doubts on its true origin (Abbott et al. 2017a). Later on, long-term observations of the afterglow signal confirmed the presence of a highly collimated, relativistic jet compatible with a short GRB, but pointing  $\approx 15 - 30$  degrees away from the line of sight (Mooley et al. 2018; Ghirlanda et al. 2019). This consolidated the idea that GRB 170817A was actually produced by a lateral portion of the outflow with limited Lorentz factor ( $< 10$ ). A promising

mechanism invoked to explain this high-energy emission, which we adopt in the present work, is the shock breakout associated with the expanding jet-cocoon system (Kasliwal et al. 2017; Gottlieb et al. 2018).

In this context, a key observable to understand the post-merger evolution is the measured  $\approx 1.74$  s delay between the GW signal and the onset of the gamma-ray emission (Abbott et al. 2017a). While a first obvious contribution to this delay is the time elapsed between the merger and the launch of the relativistic jet, additional delay accumulates as the incipient jet gradually accelerates towards ultra-relativistic velocities while piercing through the surrounding medium. In the process, a jet-cocoon system is formed and its front shock propagates through the environment, until the latter results too diluted to keep photons trapped within the shock itself (Nakar 2020). The time and radial distance characterizing the shock breakout depend on the angular distance from the jet injection axis. Moreover, the opacity of the ambient material can play an important role, as it defines the breakout condition.

When the jet is launched by the central engine, the first obstacle is represented by the dense material expelled in the post-merger phase up to the jet launch time. The mass outflow in this phase is dictated by the high temperatures reached during the

\* Corresponding author: matteo.pais@inaf.it

merger, enhanced by the growing magnetic fields with the additional contribution of neutrino heating (Foucart 2023, and refs. therein). The time it takes for the jet to be launched is a critical parameter of the problem, regulating how massive and extended this post-merger outflow component can be (e.g., Pavan et al. 2025). Beyond the latter, a second obstacle is represented by the material ejected dynamically during the merging process, characterized by a radially decreasing density profile and increasing velocity (e.g., Bauswein et al. 2013; Hotokezaka et al. 2013). The bulk of the dynamical ejecta can reach velocities as high as  $\approx 0.8c$  (e.g., Radice et al. 2018), surrounded by an even faster, extremely low density layer with dynamically irrelevant mass and energy. While the final properties of the escaping jet are mostly determined by the interaction with the denser post-merger outflows, a proper description of the bulk of the dynamical ejecta up to the fast outer tail becomes crucial in the investigation of the angle-dependent GW-EM delay, since the corresponding optical depth can strongly affect the exact time and radius of the shock breakout (e.g., Gutiérrez et al. 2025).<sup>1</sup>

In the present work, we investigate the origin of the GW-EM delay in GW170817-like BNS mergers, by means of special relativistic magnetohydrodynamic (RMHD) simulations of incipient jets launched at a given time after merger and propagating through *realistic* post-merger environments. The latter are based on the results of general relativistic MHD (GRMHD) simulations of BNS mergers by Ciolfi (2020) and combine the directly imported post-merger outflow component with dynamical ejecta faithfully reconstructed up to the fast outer tail from the original mass outflows at a radial distance of 300 km. The evolution of the jet-environment system and the propagation of the jet-driven shock is initially followed in 3D, and then continued in 2D by imposing axisymmetry. By monitoring the optical depth ahead of the shock front, we establish when the breakout condition is satisfied and thus determine the resulting GW-EM delay depending on the angular distance from the jet injection axis and the opacity of the ambient medium. Furthermore, we compute the isotropic-equivalent bolometric luminosity of the shock-breakout emission, assuming that the thermal energy within the shock is fully converted into observable radiation. We explore the effects of varying the physical model in terms of jet launch time and luminosity and compare our results with the properties of GRB 170817A, highlighting the potential of the GW-EM delay as a diagnostic of jet propagation scenarios.

The paper is organized as follows. In Section 2, we describe the numerical setup and methodology, including the construction of the initial conditions for the environment, the jet-launching prescription, and the extension of the evolution in 2D after the jet engine activity is switched off (see below). The same Section also presents our different models and the prescription adopted to identify the shock front and the breakout condition. Section 3 describes the dynamical evolution of the system, while in Section 4 we present in detail the results in terms of GW-EM delay and isotropic-equivalent bolometric luminosity, also comparing with GW170817/GRB 170817A. Finally, Section 5 summarizes our main findings and elaborates on their implications for interpreting GW-EM delays in future multi-messenger observations.

<sup>1</sup> Capturing the evolution of dynamical ejecta up to their outer front is a challenge in BNS merger simulations, due to the relatively high numerical density floor employed. Only recently, the use of a much lower density floor with rapidly decreasing radial profile has proven effective in overcoming the problem (Kalinani et al. 2026, and refs. therein).

## 2. Simulation Setup and Methods

Our study is based on simulations performed with the publicly available RMHD module of the PLUTO code (v4.4-patch3, Mignone et al. 2007), following two sequential steps. First, we inject a relativistic jet into a realistic post-merger environment, directly imported from the outcome of a GRMHD BNS merger simulation (see Section 2.1), and evolve the system in full 3D. During this initial phase, we follow the jet-environment interaction up to  $t = 0.6$  s after jet launch, corresponding to twice the characteristic decay timescale of the jet injection luminosity (Section 2.2). At this point, the jet has crossed the densest regions of the environment, consisting of the post-merger outflows driven by the massive neutron star (MNS) remnant at the center. To track the subsequent evolution over an order of magnitude longer timescale, we construct an azimuthal average of the system weighted by the energy density and continue evolving under the assumption of axial symmetry (Section 2.4). The resulting 2D description allows us to dramatically increase the resolution while extending the radial domain up to the scales where the flow approaches homologous expansion ( $t \gtrsim 10 - 20$  s).

In the following subsections, we describe in detail the initial data and 3D grid setup (Sect. 2.1), the jet injection prescription (Sect. 2.2), our different models and the numerical methods employed for the evolution (Sect. 2.3), and the procedure used to continue the evolution in 2D (Sect. 2.4). Finally, we discuss the methods used to follow the propagation of the shock front and to establish the angle-dependent breakout condition (Sect. 2.5).

### 2.1. Initial data and grid setup

Following Pavan et al. (2021, 2023, 2025), the 3D simulations are carried out in spherical coordinates  $(r, \theta, \phi)$  with an inner excised region of radius  $r_0 = 380$  km, outside of which general relativistic effects can be neglected, and with the original orbital axis of the BNS, corresponding to jet injection axis, oriented orthogonally to the coordinate polar axis. The tilted coordinates  $(r, \Theta, \Phi)$  for which the corresponding polar axis is instead aligned with the jet injection axis are linked to the spherical coordinates of the simulation  $(r, \theta, \phi)$  via the expressions reported in Appendix A.

The radial domain extends up to  $r_{\max} = 2.5 \times 10^6$  km, with logarithmic spacing in  $r$  and uniform angular spacing in  $\theta \in [0.1, \pi - 0.1]$  rad and  $\phi \in [0, \pi]$ . Note that we evolve only half of the full 3D domain, corresponding to the northern side of the system, as in the reference BNS merger simulation. The extension of the domain along  $\theta$  is chosen to avoid the polar axis singularity. The resolution is set to  $N_r \times N_\theta \times N_\phi = 768 \times 256 \times 256$ , yielding  $\Delta r \approx r\Delta\theta \approx r\Delta\phi \approx 4.4$  km at the excision radius ( $r = 380$  km).

We consider two initial environments where the jet is injected, based on the same ones employed in Pavan et al. (2025) (hereafter P25), which are in turn built on a GRMHD BNS merger simulation of Ciolfi (2020). The corresponding jet injection times are  $t_j = 185$  ms and 385 ms after merger, respectively.

The outer environment, outside the front of the MNS-driven outflows, consists of material dynamically expelled during the merger process, i.e. the dynamical ejecta. Since the original BNS merger simulation employed a uniform and rather high density floor ( $6.3 \times 10^4$  g cm<sup>-3</sup>), such ejecta were suppressed above distances of  $\sim 1000$  km. In order to include a faithful description of dynamical ejecta up to the fast low-density tail at their front, which is a key ingredient in the present investigation, we reconstruct this component consistently with the merger simulation, employing the original matter outflows up to a reliable distance of 300 km. This reconstruction, detailed in Appendix B, takes in-

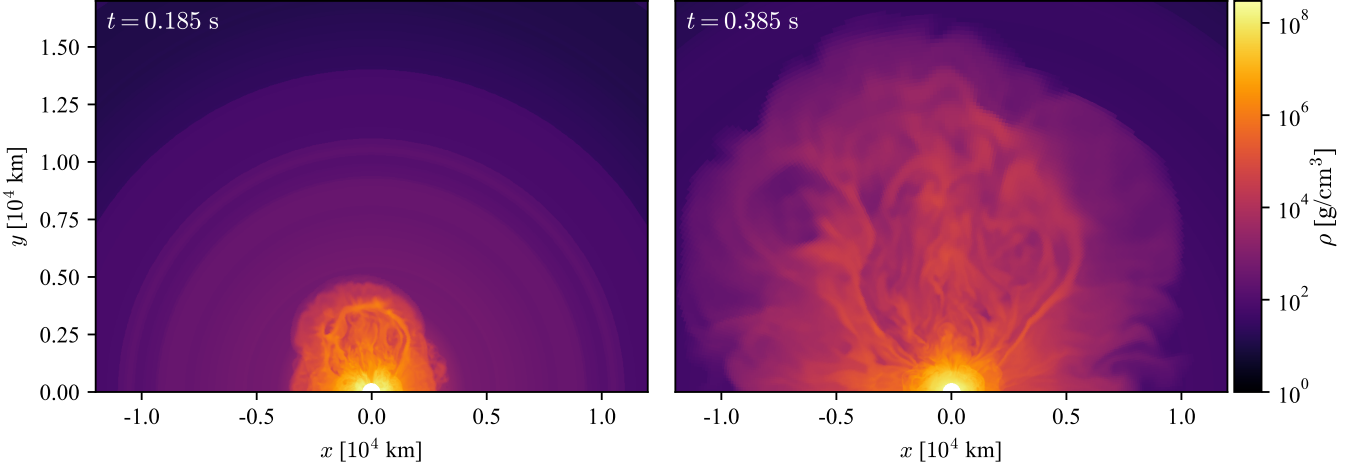


Fig. 1: Meridional view of rest-mass density at the time of jet injection for model **A** (left) and for models **B** and **C** (right), namely at 185 ms and 385 ms after merger, respectively.

put from the matter profiles along the orbital axis (positive  $z$ -axis of the merger simulation) and then assumes spherical symmetry of the dynamical ejecta. For the late-time evolution of the jet, we are indeed mostly interested in reproducing well the ejecta distribution around the orbital axis. For reconstructing the dynamical ejecta above 300 km distance, we simulate their expansion substituting the original high-density floor with a much lower one, having radial profile decreasing as  $r^{-6.5}$ . This choice has proven effective in removing floor effects on the jet evolution up to very large scales (Pavan et al. 2023).

The initial environments adopted in our 3D simulations are thus the same employed in P25 up to the maximum extension of the MNS-driven outflows (along each individual angular direction), while in the outer part we substitute the original data with the reconstructed dynamical ejecta surrounded by the very tenuous material corresponding to the new density floor decreasing as  $r^{-6.5}$ . The transition, occurring along each direction at the radius where the original density becomes smaller than the one of the reconstructed dynamical ejecta, is smooth everywhere and ensures continuity in density, pressure, and velocity. The resulting density distributions of the two initial environments in the meridional plane are shown in Figure 1. We refer to Appendix B and Figure B.2 for 1D radial profiles of density, velocity, and pressure of the reconstructed dynamical ejecta.

## 2.2. Jet injection prescription

The jet is injected at the excision radius  $r_0$  within a fixed half-opening angle of  $\theta_j = 10^\circ$ , following the prescription described in Appendix C. The one-sided jet luminosity is

$$L_j = 2\pi r_0^2 \int_0^{\theta_j} \left[ \rho_j h_j^* c^2 \Gamma_j^2 \beta_j^r - B_j^r (\boldsymbol{\beta}_j \cdot \mathbf{B}_j) - \Gamma_j^2 (\boldsymbol{\beta}_j \cdot \mathbf{B}_j)^2 \beta_j^r \right] c \sin \Theta d\Theta, \quad (1)$$

where  $\boldsymbol{\beta}$ ,  $\mathbf{B}$ , and  $\rho$  are velocity in units of  $c$ , magnetic field, and rest-mass density, respectively. The subscript “j” denotes quantities associated with the jet injection. In the above expression, we impose a constant and  $\Theta$ -independent Lorentz factor  $\Gamma_j = 3$  and  $h_j^* = (1 + \sigma_j)h_j = 100$ , where  $h_j$  is the specific enthalpy and  $\sigma_j$  the local magnetization (see Appendix C.1). In the tilted reference frame, the jet has a radial and azimuthal magnetic field,

with the former being  $\Theta$ -independent and the latter following the same dependence on  $\Theta$  as in Martí (2015) and Geng et al. (2019) (see also Pavan et al. 2023):

$$B^r = B_{\text{ratio}} B_0, \quad B^\Phi(\Theta) = B_0 \frac{2(\Theta/\theta_m)}{1 + (\Theta/\theta_m)^2}, \quad (2)$$

where  $B_0$ ,  $B_{\text{ratio}}$ , and  $\theta_m$  are constant. The jet’s magnetic-field configuration is then fully specified by imposing  $\theta_m = 0.4\theta_j$ , and setting the overall field strength through  $B_0 = 1.55 \times 10^{13}$  G and the ratio of radial to azimuthal field via  $B_{\text{ratio}} = 0.5$ . Finally, the rest-mass density profile within the jet,  $\rho_j(\Theta)$ , is found by imposing transverse equilibrium and choosing a value for  $L_j$  (see Appendix C.2).

In our description, we consider a jet luminosity that decays exponentially in time with characteristic timescale  $\tau_L = 0.3$  s, namely  $L_j(t) = L_0 \exp[-(t - t_j)/\tau_L]$  with  $L_0 \equiv L_j(t_j)$ . Such a time dependence is enforced by assuming that  $\rho_j$  and  $\mathbf{B}_j$  decrease exponentially with characteristic timescales of  $\tau_L$  and  $2\tau_L$ , respectively.

## 2.3. Models and numerical methods

In this study, we consider three models varying the initial jet luminosity and the jet injection time (since merger):

- **Model A**:  $t_j = 0.185$  s,  $L_0 = 10^{51}$  erg s $^{-1}$ ,
- **Model B**:  $t_j = 0.385$  s,  $L_0 = 10^{51}$  erg s $^{-1}$ ,
- **Model C**:  $t_j = 0.385$  s,  $L_0 = 5 \times 10^{51}$  erg s $^{-1}$ .

The above  $L_0$  values, along with the other fixed parameters (see previous Section), correspond to weakly magnetized jets, for which the magnetic contribution to the luminosity is

$$\Sigma_j \equiv \frac{L_j - L_{\text{HD}}}{L_j} \approx 5.51\% \left( \frac{L_j}{10^{51} \text{ erg s}^{-1}} \right)^{-1}. \quad (3)$$

where  $L_{\text{HD}}$  denotes the purely hydrodynamic contribution to the jet luminosity.

The evolution is carried out using the generalized First Order Centred (FORCE) Riemann solver (Toro & Titarev 2006; Mattia & Mignone 2021), fifth-order piecewise parabolic reconstruction (Mignone 2014), and third-order Runge–Kutta

time stepping. We chose a Taub-Matthews equation of state (Mignone & McKinney 2007), reproducing an ideal gas law with adiabatic index  $\gamma = 4/3$  in the ultrarelativistic limit and with  $\gamma = 5/3$  in the non-relativistic limit, with a smooth transition at intermediate regimes. The divergence-free constraint for the magnetic field is enforced using the Hyperbolic Divergence Cleaning (Dedner et al. 2002), while retaining a cell-centered representation of the primary fluid variables (including the magnetic field) in our simulations. A vector-force Newtonian field is employed to simulate the gravitational pull from the central compact object, setting its mass to  $M_0 \approx 2.596 M_\odot$  as in the reference BNS merger simulation. ‘Outflow’ boundary conditions are imposed at the outer radial boundary and the  $\theta$  boundaries, while the conditions are periodic along the  $\phi$  direction. The inner radial boundary conditions are user-defined within the chosen half-opening angle, allowing for the jet injection according to the prescription given in the previous subsection (Sect. 2.2), and set as outflow outside of it. During the evolution, we keep track of the fraction of jet material in each computational cell via the scalar  $Q_j$ , passively advected with the fluid.

#### 2.4. Extending the evolution in axisymmetry

At the end of the 3D evolution, once the system reaches  $t = 0.6$  s after jet launch, we switch off the jet engine, impose an outflow condition for the inner radial boundary, and further continue the evolution in 2D and axisymmetry after performing an azimuthal average of the 3D data.

Before the axisymmetrization step, all fluid quantities are mapped in the tilted coordinate system  $(r, \Theta, \Phi)$ , in which the polar axis is aligned with the jet injection axis. The azimuthal average (i.e. along the  $\Phi$  coordinate) is then computed by weighting each quantity with the local energy density (including kinetic, thermal, and magnetic energy densities). This choice enhances the imprint of the energetically dominant jet material while suppressing contributions from slower, less relevant regions of the outflow. Moreover, the total energy of the system is better preserved (order  $\sim 1\%$  lower than the original one in 3D) with respect to the non-weighted average (one order of magnitude larger discrepancy). In this framework, the flow is evolved on a 2D spherical grid while retaining the evolution of  $v^\Phi$  and  $B^\Phi$  under periodic boundary conditions.

Since the relevant part of the jet and cocoon structure is confined within  $\Theta < 45^\circ$  from the jet injection axis, we restrict the angular domain to  $\Theta \in [0, 45^\circ]$ . At the same time, we take advantage of the significantly reduced computational cost of 2D simulations to increase the resolution by a factor of 8 while retaining the original cell aspect ratio (i.e.  $\Delta r \approx r\Delta\Theta$ ), achieving a finest spacing of  $\approx 0.55$  km at  $r = 380$  km. The corresponding 2D grid is covered by 6144 and 256 points along the radial and  $\Theta$  coordinates, respectively.

During the evolution, the inner radial boundary is moved from 380 km to larger distances at specific times, depending on the considered case. In particular, for model **A**, the inner radius is moved to  $10^4$  km at  $t - t_j = 1.8$  s, while for model **B** and **C**, it is moved to  $10^4$  km at  $t - t_j = 0.9$  s, and subsequently to  $10^5$  km at  $t - t_j = 5$  s. In these steps, the number of grid points is unchanged: the grid remains identical except that points are removed from the inner region and added to the outer region (increasing  $r_{\max}$  accordingly). The inner region that is cut away has no relevance for the dynamics of the jet and cocoon system we are interested in. Moreover, the smallest grid spacing increases, with consequent speedup of the simulated evolution. Finally, the farther away

outer boundary allows us to cover longer physical times before the boundary itself is reached by the outflowing material.

#### 2.5. Shock front identification and breakout condition

To locate the position of the forward shock at each time and angle, we employ the multi-criterion shock-finding procedure described in Appendix D (see also Mignone et al. 2011; Gupta et al. 2019, 2021). In order to establish when and where the shock breakout occurs along a given polar angle  $\Theta$ , we monitor the optical depth at the location of the shock front until the following relativistic shock-breakout condition is satisfied (Nakar 2020):

$$\tau(r_{\text{sh}}) \simeq \frac{1}{\beta'_{\text{sh}}} = \frac{1 - \beta_{\text{sh}}\beta_{\text{ej}}}{\beta_{\text{sh}} - \beta_{\text{ej}}} \approx \frac{\Gamma_{\text{sh}}^2 + \Gamma_{\text{ej}}^2}{\Gamma_{\text{sh}}^2 - \Gamma_{\text{ej}}^2}, \quad (4)$$

where  $\beta'_{\text{sh}}$  is the velocity of the shock (in units of  $c$ ) in the local rest frame of the unshocked dynamical ejecta, while  $\beta_{\text{sh}}$  and  $\beta_{\text{ej}}$  are the velocities of the shock and the unshocked dynamical ejecta in the ‘lab’ frame, i.e. the rest frame of our computational grid and of the observer (with  $\beta_{\text{sh}} > \beta_{\text{ej}}$ ).

For a given radial density profile, the optical depth at the shock front is given by (Abramowicz et al. 1991)

$$\tau(r_{\text{sh}}) = \kappa \int_{r_{\text{sh}}}^{\infty} \rho(\tilde{r}') d\tilde{r}' = \kappa \int_{r_{\text{sh}}}^{\infty} \rho(\tilde{r}) \Gamma(\tilde{r}) [1 - \beta(\tilde{r})] d\tilde{r}, \quad (5)$$

where  $\kappa$  is the (frequency independent) opacity,  $\tilde{r}'$  and  $\tilde{r}$  are the radial length in the local comoving frame of the ejecta and in the lab frame, respectively, and  $\Gamma(\tilde{r})$  and  $\beta(\tilde{r})$  are the local Lorentz factor and velocity in units of  $c$  as seen in the lab frame. As a fiducial value, we take  $\kappa = 0.16$  cm<sup>2</sup>/g (see Nakar 2020), while in Section 4.4 we discuss the effects of varying  $\kappa$ .

### 3. Evolution Results

In this Section, we present the time evolution of our models **A**, **B**, and **C** (see Section 2.3). The three models allow us to explore the dependence of jet propagation and breakout on both the launch time (with respect to merger time) and the injected power, while keeping fixed the other incipient jet parameters.

We first describe the initial 3D evolution up to 0.6 s after jet launch, which captures the jet interaction with the dense post-merger outflows and the formation of the jet–cocoon structure, and then consider the subsequent axisymmetric evolution extending to  $t - t_j = 20$  s, following the long-term propagation of the forward shock into the dilute dynamical ejecta.

#### 3.1. 3D evolution up to 0.6 seconds

During its early propagation, the incipient jet has to pierce through the dense post-merger outflows driven by the MNS remnant, transferring part of its energy to the surrounding medium and forming a jet-cocoon structure. Upon overcoming the outer radius of the MNS-driven outflows, the jet-cocoon front starts propagating across the much less dense dynamical ejecta, rapidly accelerating and laterally expanding.

Figure 2 shows meridional slices of the total energy density  $e_{\text{tot}}$  (including kinetic, thermal, and magnetic energy densities, but not the rest-mass contribution) at  $t = 0.6$  s after jet launch for the three models. In model **A** (early launch, moderate luminosity), the jet emerges from a comparatively less extended MNS-driven environment, starting earlier its propagation across

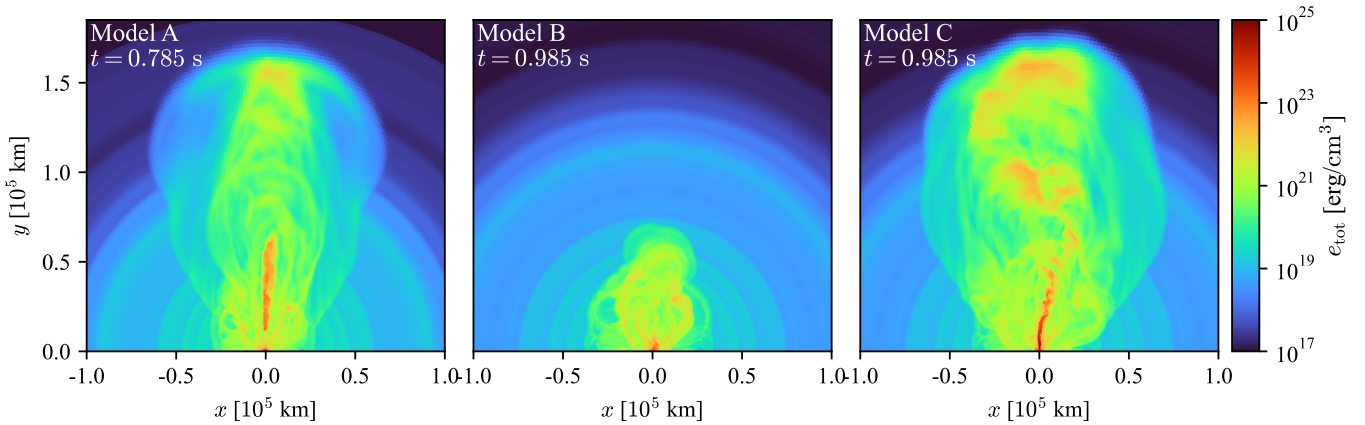


Fig. 2: Meridional view of the total energy density  $e_{\text{tot}}$  at 0.6 s after the jet injection time for models **A**, **B**, and **C** (left to right). The time reported in each panel is the time after merger.

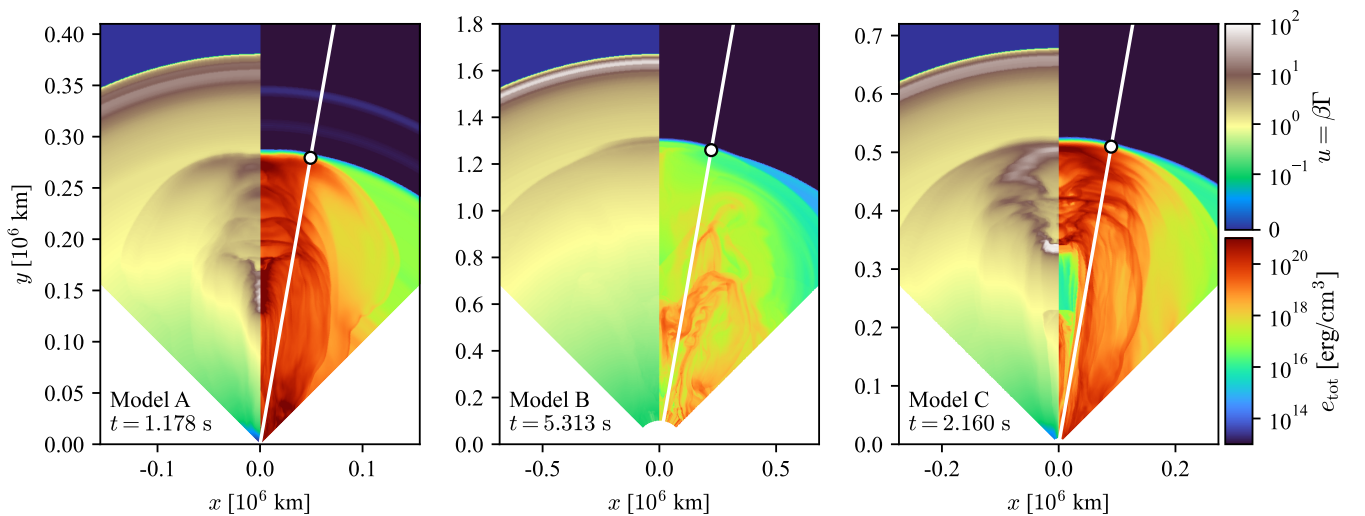


Fig. 3: Meridional view of the proper velocity  $u = \beta\Gamma$  (left half of the panels) and the total energy density  $e_{\text{tot}}$  (right half of the panels) for the three models **A**, **B**, and **C** at the time when the shock breakout occurs along a radial direction  $10^\circ$  away from the jet injection axis. The spatial scale in each panel varies depending on the model. The white solid line shows the direction at  $10^\circ$ , and the white circle marks the breakout radius along that line.

the outer dynamical ejecta. This results in a rather axisymmetric structure, with a narrow energetic jet core surrounded by the less energetic cocoon. In contrast, the jet of model **B** (later launch time) propagates through a significantly more extended (and massive) MNS-driven environment, losing a larger fraction of its energy while struggling to pierce through. As a result, this jet shows clear signs of partial choking, and emerges without a well-defined jet core. The higher luminosity of model **C** partially compensates for the later injection time, producing a more energetic jet-cocoon structure, but less collimated and axisymmetric than model **A**.

By 0.6 s, the evolution has reached a stage where the global jet-cocoon morphology and angular structure have largely been established. At the same time, the energy injection from the central engine is nearly over (luminosity is a factor  $\approx 7.4$  lower than the initial value), allowing us to switch off the latter for the further evolution without affecting the dynamics at the front of the expanding jet-cocoon structure.

### 3.2. Axisymmetric evolution

We follow the subsequent evolution via 2D axisymmetric simulations as described in Sect. 2.4. The transition to axisymmetry preserves the essential features established during the 3D phase — namely the jet-cocoon morphology and energetics — while enabling much higher resolution and larger dynamical range at a significantly reduced computational cost.

Figure 3 shows, for each model, the proper velocity  $u = \beta\Gamma$  and total energy density  $e_{\text{tot}}$  at the time at which the shock breakout occurs along a radial direction  $10^\circ$  away from the jet injection axis. As the flow expands into the outer dynamical ejecta, the forward shock accelerates and gradually approaches a self-similar structure. The timing and radius of the breakout differ substantially across the three models. Model **A**, with early jet injection into a less extended environment, exhibits a much smaller breakout radius  $r_{\text{bo}}$  and earlier breakout time  $t_{\text{bo}}$  compared to model **B**, while model **C**, whose enhanced luminosity partially compensates for the more extended environment, exhibits intermediate values of  $r_{\text{bo}}$  and  $t_{\text{bo}}$ . We also note that the Lorentz factor at

breakout,  $\Gamma_{\text{bo}}$ , is smaller than 10 for all three models. Beyond the outer radius of the bulk of the dynamical ejecta, at  $r > r_{\text{bo}}$ , there is an extremely low density and energetically negligible portion of material whose front reaches  $\Gamma > 10$ . As discussed below, this material does not contribute to the optical depth and plays no role in our investigation.

In Figure 4, we present the radial profiles of total energy density, Lorentz factor, and rest-mass density along the direction  $10^\circ$  away from the jet injection axis at the corresponding breakout times (i.e. the same times indicated in Fig. 3). The shock front radius  $r_{\text{bo}}$  is marked by a dashed vertical line. All models exhibit a sharp, well-defined shock front, as seen in the energy density profile. For model **B**, the rest-mass density drop prior to the shock front is much more gradual and the peak of the velocity at the front is significantly lower. These features reflect the fact that, in this case, the jet is significantly choked (see also Fig. 3).

For all three models, looking at distances larger than  $r_{\text{bo}}$ , the profiles clearly show that the energy content of the outer material is negligible, despite the presence of a rather high peak in Lorentz factor. Moreover, due to the extremely low densities, the contribution of this material to the optical depth is also negligible.

#### 4. GW-EM delay and shock-breakout luminosity

In this Section, we compute the time interval between the detection of the GW signal (emitted at the merger time) and the arrival of the first photons produced during the shock breakout of the jet–cocoon system, depending on the observing angle. Moreover, we compute the isotropic-equivalent bolometric luminosity of the signal, under the assumption that the thermal energy of the shocked material is entirely converted into radiation.

##### 4.1. Time evolution and angular dependence of the delay

We first consider the delay along a fixed angular direction  $\Theta$ , given by  $t_{\text{bo}} - r_{\text{bo}}/c$ , where  $t_{\text{bo}}$  is the time since merger at which breakout occurs and thus photons are free to propagate at the speed of light towards the observer.

In Table 1, we summarize the results for our three models at  $\Theta = 5^\circ$  (i.e. close to the jet injection axis), in terms of  $r_{\text{bo}}$ ,  $t_{\text{bo}}$ ,  $\Gamma_{\text{bo}}$  and the delay itself ( $\Delta t_{\text{GW-EM}}$ ). We note that the given delays include the time interval between merger and jet launch. Once this time interval is subtracted, the delay due to the jet propagation until breakout becomes about 60, 660, and 40 ms, respectively. We thus infer that, for models **A** and **C**, in which either a less massive and extended environment or a factor 5 higher luminosity significantly enhances jet propagation, the total GW–EM delay is largely determined by the time interval between merger and jet launch, which accounts for about 77% and 92% of the total delay, respectively. Conversely, for model **B**, in which jet propagation is less efficient, this interval accounts for only 37% of the total delay, with the propagation itself providing the largest, though comparable, contribution.

In Figure 5, we illustrate how the GW-EM delay accumulates over time until breakout, for several polar angles (from  $5^\circ$  to  $30^\circ$ , at steps of  $5^\circ$ ) and for the different models. Each profile ends at the shock breakout time, represented by a square marker. We note that the delay, in the early phase, is not necessarily monotonically increasing. This is due to the non-radial component of the shock front propagation: along a given polar angle, when a more advanced and laterally expanding shock front becomes detectable, the reference radius for computing the delay can move

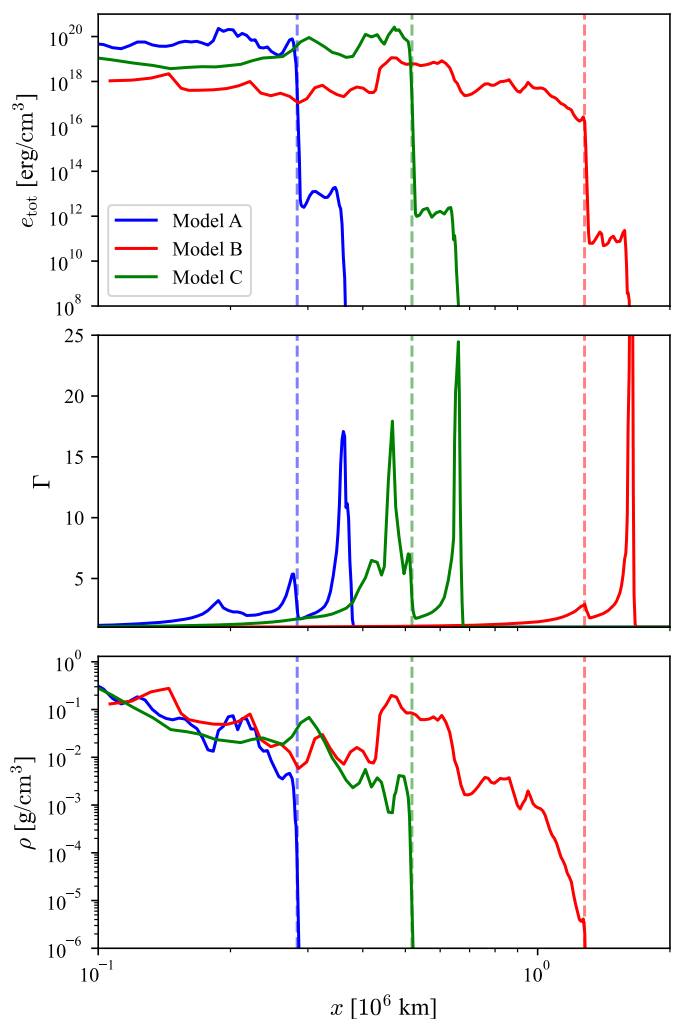


Fig. 4: 1D profiles of the energy density  $e_{\text{tot}}$  (top), Lorentz factor (middle), and rest-mass density (bottom) along the radial direction  $10^\circ$  away from the jet injection axis, at the corresponding shock breakout time (see Fig. 3). Different colors refer to different models: **A** (blue), **B** (red), and **C** (green). For each model, a vertical dashed line marks the breakout radius.

Model	$t_j$ [s]	$L_{0,51}$	$r_{\text{bo},10}$	$t_{\text{bo}}$ [s]	$\Gamma_{\text{bo}}$	$\Delta t_{\text{GW-EM}}$ [s]
A	0.185	1	2.8	1.17	3.7	0.24
B	0.385	1	12.2	5.31	3.0	1.04
C	0.385	5	5.1	2.11	5.4	0.42

Table 1: Shock breakout properties at  $5^\circ$  from the jet injection axis, for models **A**, **B**, and **C**, having different jet launch time  $t_j$  (since merger time) and initial luminosity  $L_0$  (expressed in units of  $10^{51}$  erg/s). For each model, we report breakout radius  $r_{\text{bo}}$  (expressed in units of  $10^{10}$  cm), breakout time since merger  $t_{\text{bo}}$ , Lorentz factor at breakout  $\Gamma_{\text{bo}}$ , and GW-EM delay time  $\Delta t_{\text{GW-EM}}$ . The assumed opacity is  $\kappa = 0.16$  cm<sup>2</sup>/g.

ahead faster than the speed of light (while no fluid element is violating causality).

The thin gray lines in Fig. 5 trace the outer edge of the bulk of the dynamical ejecta, which are isotropic and move self-similarly with constant velocity  $v_{\text{ej}} \approx 0.8 c$ . The corresponding radius is

$$R_{\text{ej}}(t) = 9.24 \times 10^9 \text{ cm} \left( \frac{t}{0.385 \text{ s}} \right), \quad (6)$$

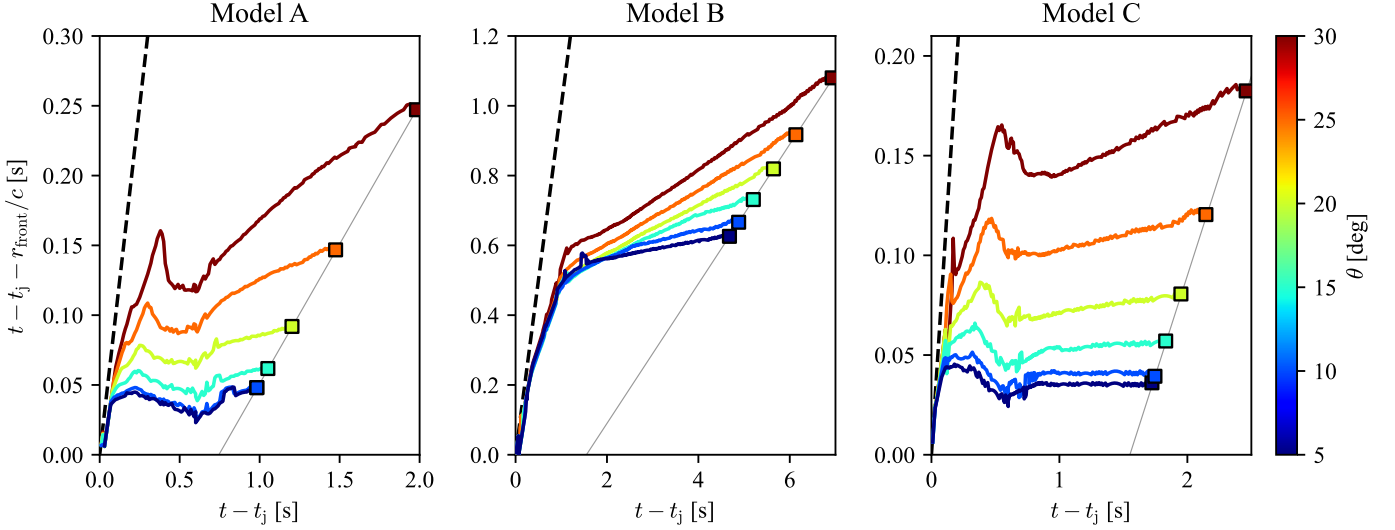


Fig. 5: Delay accumulated over time by the jet-cocoon shock front (at  $r = r_{\text{front}}$ ) with respect to the GW signal, excluding the jet launch time  $t_j$ , along different polar angles (color-coded) and for the different models. An opacity of  $\kappa = 0.16 \text{ cm}^2/\text{g}$  is assumed. The colored squares mark the shock breakout. The dashed black line in each panel represents the delay that would be accumulated in the limit of a shock front advancing with zero velocity (i.e. at rest, with constant  $r_{\text{front}} = 380 \text{ km}$ ). The thin gray line is the outer radius of the bulk of the dynamical ejecta, expanding self-similarly at about  $0.8c$ .

where  $t$  is the time since merger. Shock breakout along a given direction occurs when the jet-cocoon shock front reaches such an edge.

After a first early phase (at  $\geq 1 \text{ s}$  since jet launch), the jet-cocoon shock front can be approximated as an expanding ellipsoid, with semi-major axis  $r_{\parallel}(t) = r_0 + v_{\parallel}(t - t_j)$  and semi-minor axis  $r_{\perp}(t) = v_{\perp}(t - t_j)$ , with  $r_0 = 380 \text{ km}$  and where  $v_{\parallel}$  and  $v_{\perp}$  are the expansion velocities along the jet injection axis and along the direction orthogonal to it, respectively. The corresponding ellipsoidal radius is

$$r_{\text{ellipsoid}}(t, \Theta) = \left[ \frac{\cos^2 \Theta}{r_{\parallel}^2(t)} + \frac{\sin^2 \Theta}{r_{\perp}^2(t)} \right]^{-1/2}. \quad (7)$$

The condition  $r_{\text{ellipsoid}}(t, \Theta) = R_{\text{ej}}(t)$  determines a fourth-order polynomial in  $t$  whose real positive root is the shock breakout time  $t_{\text{bo}}(\Theta)$ . The on-axis breakout is easily found imposing  $\Theta = 0$  and solving for  $t$ :

$$t_{\text{bo}}(\Theta = 0) = \frac{R(t_j) - r_0}{v_{\parallel} - v_{\text{ej}}}. \quad (8)$$

Comparing the on-axis breakout time with the simulation results for each model, we can determine  $v_{\parallel}$ , while  $v_{\perp}$  is left as a free parameter. The values for  $v_{\parallel}$  are found to be  $(0.963, 0.865, 0.979) c$  for models **A**, **B**, and **C**, respectively. Then, fixing  $v_{\perp}$  to  $(0.710, 0.789, 0.800) c$  for the three models, we are able to match all breakout times up to  $30^\circ$  within a 5% error. This shows that a simple analytic description, without explicitly modelling the complex jet dynamics and momentum balance equation for jets embedded in an expanding medium (Hamidani & Ioka 2021), can capture the main features of the jet-cocoon shock expansion at times  $\geq 1 \text{ s}$  since jet launch.

#### 4.2. Relativistic beaming

At breakout, the relativistic beaming confines the radiation emitted from the shock front at  $\Theta$  within a half-opening angle  $\theta_{\text{beam}}$ , where  $\sin \theta_{\text{beam}} = 1/\Gamma_{\text{bo}}(\Theta)$  and  $\cos \theta_{\text{beam}} = \beta_{\text{bo}}(\Theta)$ . The first

shock breakout photons received by an observer at  $\Theta = \theta_{\text{obs}}$  may originate from a portion of the shock front moving along a different polar angle, and characterized by a smaller  $t_{\text{bo}}$ , as long as the observer direction is within the beaming angle of the emitting region. Since  $t_{\text{bo}}$  is monotonically increasing with  $\Theta$ , for a given  $\theta_{\text{obs}}$  we compute the delay of the first photons emitted from the shock front at a  $\Theta$  such that  $\Theta + \theta_{\text{beam}}(\Theta) = \theta_{\text{obs}}$ , and compare with the delay of the photons emitted at  $\Theta = \theta_{\text{obs}}$ . The actual delay observed will be the lesser of the two.

In Figure 6, for each model, we report both delays (front-view and beaming-corrected) depending on  $\theta_{\text{obs}}$ , and mark with a continuous thicker line minimum of the two (representing the actually observed delay). For  $\theta_{\text{obs}} \geq 20^\circ$ , photons emitted closer to the jet axis arrive earlier and this effect results in a significantly weaker dependence of the delay itself on  $\theta_{\text{obs}}$ .

Overall,  $\Delta t_{\text{GW-EM}}$  is found to depend rather poorly on the observer direction: going from  $0^\circ$  to  $30^\circ$ , we find variations of  $\approx 0.3 \text{ s}$  for model **B** and  $< 0.1 \text{ s}$  for models **A** and **C**. This property makes  $\Delta t_{\text{GW-EM}}$  a very powerful diagnostic to distinguish among models. In particular, when comparing to an observation with precise delay determination but a wide range of possible viewing angles (like in the case of GW170817), any model can be confidently excluded unless the narrow range of possible delays is consistent with the observed one.

Taking the range  $\theta_{\text{obs}} \in [14^\circ, 28^\circ]$  as representative for GW170817 (Mooley et al. 2018, 2022), Table 2 shows for our three models the corresponding range of possible delays, to be compared with the  $\approx 1.74 \text{ s}$  of GW170817 (Abbott et al. 2017a). In all cases, variations are within 15% and compatibility with the 2017 event can be excluded with full confidence. In terms of delay only, model **B** is significantly closer to  $1.74 \text{ s}$ , although still inconsistent.

#### 4.3. Emitted luminosity

We compute the EM emission associated with shock breakout using the procedure described in detail in Appendix E. Here we summarize the essential elements of such a procedure. For a given observing angle  $\theta_{\text{obs}}$ , the shock-breakout time  $t_{\text{bo}}$  is de-

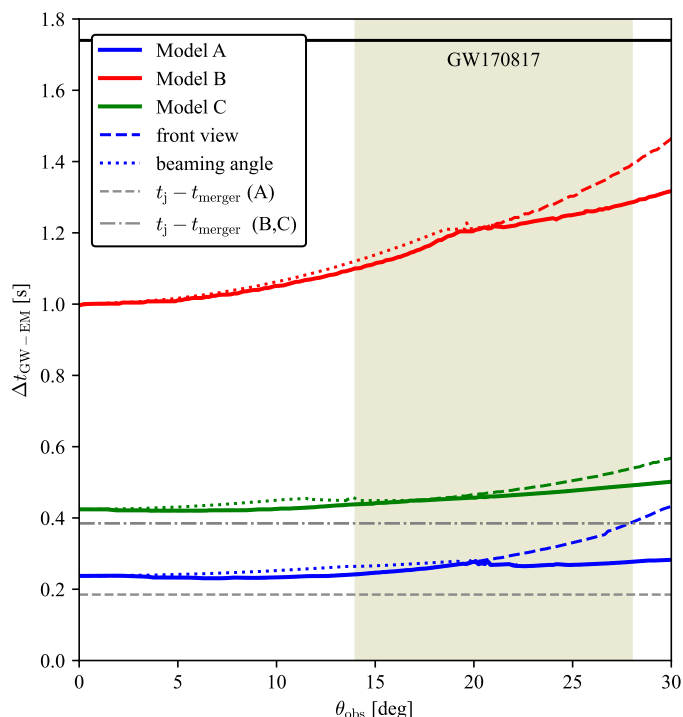


Fig. 6: Time delay between the GW and the shock breakout signal ( $\Delta t_{\text{GW-EM}}$ ) as a function of the observing angle  $\theta_{\text{obs}}$ , for our three models (represented in different colors) and assuming an opacity of  $\kappa = 0.16 \text{ cm}^2/\text{g}$ . The dashed and dotted lines show, respectively, the delays computed for photons emitted from a shock region at either (i) a polar angle equal to  $\theta_{\text{obs}}$  or (ii) the smallest polar angle for which the relativistic beaming cone still includes the observer direction. The minimum of the two, indicated with a continuous thicker line, is the actual delay (see text for details). The shaded region marks the observationally inferred viewing-angle range for GW170817. The grey horizontal lines indicate the jet launching time relative to the merger time for each model, as reported in the legend.

defined as the time at which the shock reaches the photospheric or emission radius, determined by the condition  $\tau \approx 1/\beta_{\text{sh}}'$  (see Eq. 4). After this time, photons initially trapped in the shocked material start diffusing out. The emission radius, which changes in time according to the same condition  $\tau \approx 1/\beta_{\text{sh}}'$ , recedes in time (moving backwards in the frame comoving with the shock front) as radiation escapes from progressively deeper regions of the flow. Assuming that the signal is powered by the thermal energy contained within the emitting layer, the contribution from each portion of the latter in a given timestep will correspond to the increase of thermal energy outside the emission radius.

To account for non-radial contributions, at each timestep we divide the emitting layer in portions that, projected on a plane orthogonal to the observer's direction, correspond to  $(2N + 1)^2$  equal squares of side length  $\lambda = R/N$ , where  $R$  is the time-evolving radial extension of the emitting layer and  $N = 50$ . For each portion, we compute the optical depth by integrating along the observer's direction, establishing the volume containing the thermal energy that will be released in that timestep (see Fig. E.1). Moreover, we account for relativistic Doppler shifts towards the observer and for the different light travel times from each portion. As final result, we obtain the observed isotropic-equivalent bolometric luminosity  $\mathcal{L}_{\text{iso}}$  as function of the observing time  $T_{\text{obs}}$ , for the chosen  $\theta_{\text{obs}}$ .

Model	$t_j$ [s]	$L_0$ [ $10^{51}$ erg/s]	$\Delta t_{\text{GW-EM}}$ [s] for $\theta_{\text{obs, GW170817}}$
A	0.185	1	0.24 – 0.28
B	0.385	1	1.10 – 1.28
C	0.385	5	0.44 – 0.49

Table 2: Time delays between the GW and the shock breakout signal ( $\Delta t_{\text{GW-EM}}$ ) corresponding to the range of viewing angles  $\theta_{\text{obs}} \in [14^\circ, 28^\circ]$ , representative of GW170817.

The resulting  $\mathcal{L}_{\text{iso}}$  for models **A**, **B**, and **C** are shown in Figure 7 for several viewing angles  $\theta_{\text{obs}}$  (from  $5^\circ$  to  $30^\circ$  from the jet injection axis, at steps of  $5^\circ$ ). The gray shaded region marks the time interval from merger to jet launch, during which no emission is expected. In all models, the luminosity rapidly rises following shock breakout, and after reaching its peak, it decays on a sub-second timescale. Model **A** and **C** produce fast-rising emission early after jet launch, while model **B** yields a significantly delayed and broader signal, consistent with its later breakout.

The onset time of the emission with respect to the GW arrival time can be established in a model-independent way by computing  $T_{5\%}$ , i.e. the time at which the integrated luminosity corresponds to 5% of the total emitted energy. The values of  $T_{5\%}$  for the different models and viewing angles are reported in Table 3. We remark that such onset times are fully consistent with the GW-EM delays ( $\Delta t_{\text{GW-EM}}$ ) previously computed based on the shock breakout condition only (see §4.1 and §4.2).

In Figure 8, we show instead the time interval  $T_{90}$ , going from  $T_{5\%}$  to  $T_{95\%}$ , depending on the model and the viewing angle. As expected, results for models **A** and **C** are rather similar, with a  $T_{90}$  ranging from about 0.05 to 0.2 s, while for model **B** we obtain significantly larger values in the range  $\approx 0.3 - 0.7$  s, comparable to the  $\approx 0.5$  s characterizing the main peak of GRB 170817A (Goldstein et al. 2017). In addition, we note that the duration of the breakout signal is in order-of-magnitude agreement with the dynamical timescale  $r_{\text{bo}}/(\Gamma_{\text{bo}}^2 \beta_{\text{bo}} c)$ .

In terms of peak luminosities, besides the strong dependence on the viewing angle, the outcome changes by orders of magnitude among the three models (Figure 7). At  $\theta_{\text{obs}} = 15^\circ$ , for instance, model **B** reaches  $\sim 5 \times 10^{48}$  erg/s, model **A**  $\sim 2 \times 10^{50}$  erg/s, and model **C**  $\sim 10^{51}$  erg/s.

The computed  $\mathcal{L}_{\text{iso}}$  is bolometric and obtained under the assumption that all the available thermal energy is converted into radiation. In order to relate to a signal such as GRB 170817A, whose inferred isotropic-equivalent peak luminosity in the high-energy band (1 keV–10 MeV) is  $\approx 1.6 \times 10^{47}$  erg/s (Goldstein et al. 2017; Zhang et al. 2018), one would need to estimate the fraction of  $\mathcal{L}_{\text{iso}}$  that would contribute to the observed signal in the same high-energy band. Such a radiative efficiency factor,  $f_\gamma \equiv \mathcal{L}_{\text{iso}, \gamma}/\mathcal{L}_{\text{iso}}$ , is typically expected to be as low as (1–10)% (Kumar 1999). Restricting to  $\theta_{\text{obs}}$  between  $15^\circ$  and  $25^\circ$ , i.e. roughly the range of possible viewing angles consistent with GRB 170817A, the values of  $f_\gamma$  that would reconcile our three models with such a signal are:  $\sim 10^{-3} - 10^{-2}$  for model **A**,  $\sim 3 \times 10^{-2} - 10^{-1}$  for model **B**, and  $\sim 2 \times 10^{-4} - 2 \times 10^{-3}$  for model **C**. In conclusion, model **B** appears broadly consistent with the expected order of magnitude, while models **A** and **C** would require much lower  $f_\gamma$  values.

$\theta_{\text{obs}}$ [deg]	Onset time ( $T_{5\%}$ ) [s]		
	Model A	Model B	Model C
5	0.24	1.05	0.44
10	0.25	1.07	0.44
15	0.26	1.11	0.45
20	0.27	1.17	0.47
25	0.28	1.24	0.49
30	0.30	1.33	0.52

Table 3: Onset time of the shock breakout signal with respect to the GW arrival time, for the different models and viewing angles, computed as  $T_{5\%}$  (i.e. the time at which the emitted energy reaches 5% of the total).

#### 4.4. Light curves with different opacities

Figure 9 shows the isotropic-equivalent bolometric luminosity of the shock breakout emission for different models (top to bottom) and viewing angles (color-coded), as a function of the observer time  $T_{\text{obs}}$  (with the arrival time of the GW signal set to  $T_{\text{obs}} = 0$ ), where we consider two different constant values for the opacity:  $\kappa = 0.16 \text{ cm}^2/\text{g}$  (fiducial value) and ten times larger  $\kappa = 1.6 \text{ cm}^2/\text{g}$ .

We find that a factor 10 increase in opacity does not sensibly alter the onset time of the signal, altering it by  $< 1.5\%$  for all models. This indicates that the dependence of the GW-EM delay on the opacity is very weak, making such a diagnostic even more effective in comparing models with a specific observation.

Considering the overall light curves, the increased value of  $\kappa$  has some limited effects. In particular, the peak luminosity is lower by at most a factor 2 and the duration  $T_{90}$  is smaller by less than 30%.

## 5. Summary and conclusions

In this work, we investigated the time delay between the peak GW signal of a BNS merger and the onset of shock-breakout EM emission associated with a relativistic jet launched after merger and piercing through the surrounding medium. To this end, we performed RMHD simulations of jet propagation in a realistic post-merger environment, directly imported from the outcome of a previous GRMHD BNS merger simulation. Such a propagation environment includes the outer dynamical ejecta component, which plays a crucial role in regulating the shock-breakout condition and thus the corresponding breakout time and radius along any angular direction. Since this key component is suppressed by the high numerical density floor in the GRMHD simulation, we reconstructed it from the original matter outflow at 300 km distance, where no suppression has occurred yet. For simplicity, we reconstructed the 1D dynamical ejecta profile along the orbital (or jet-injection) axis, and then assumed a spherically symmetric distribution. The evolution of the system was followed in 3D up to 0.6 s (since jet launch) and then continued in 2D up to several seconds.

By varying the jet launching time (since merger) and the injected luminosity, we considered three representative models (A, B, and C) that span a range of jet-environment interaction regimes: (i) early and relatively clean breakout, (ii) slower propagation through a more extended and massive surrounding medium, (iii) relatively fast propagation through the more extended medium enabled by a higher jet power. These models allowed us to explore how different physical conditions affect both the timing and early luminosity of the shock-breakout emission.

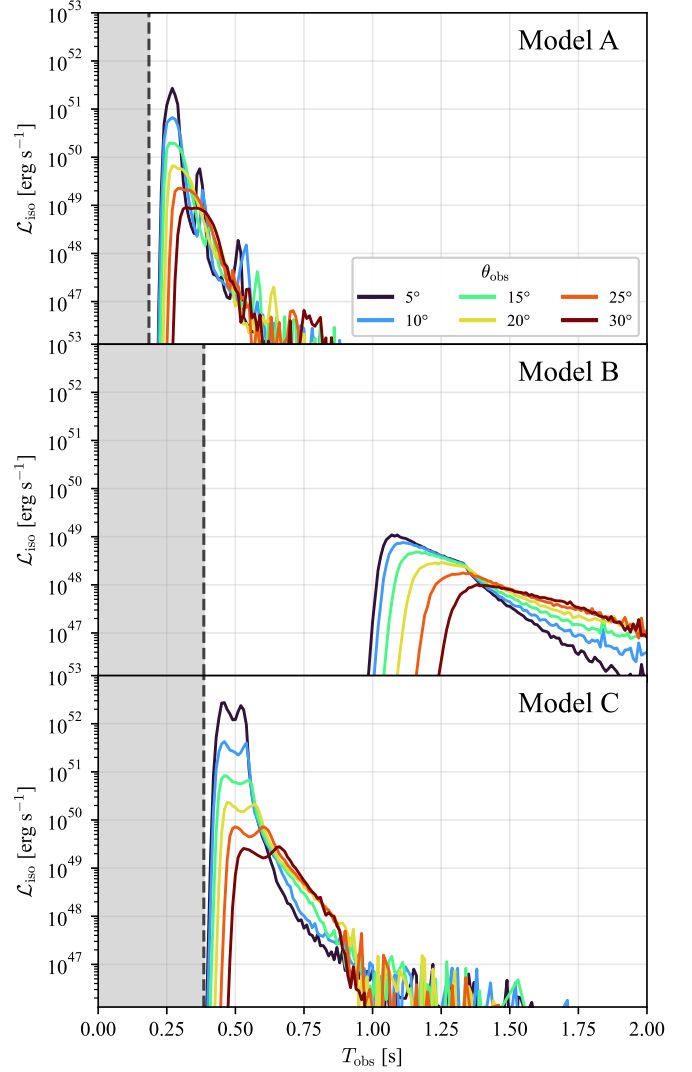


Fig. 7: Isotropic-equivalent bolometric luminosity of the shock breakout emission for different models (top to bottom) and viewing angles (color-coded), as a function of the observer time  $T_{\text{obs}}$  (where  $T_{\text{obs}} = 0$  corresponds to the arrival time of the GW signal). The gray area extending up to the black dashed vertical line corresponds to the time interval between merger and jet launch.

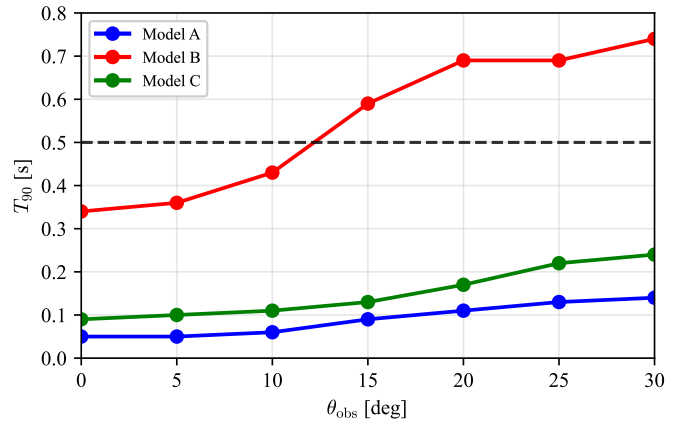


Fig. 8: Fluence time  $T_{90}$  for the different models as a function of the viewing angle. The black dashed horizontal line represents the approximate duration of the main peak of GRB 170817A.

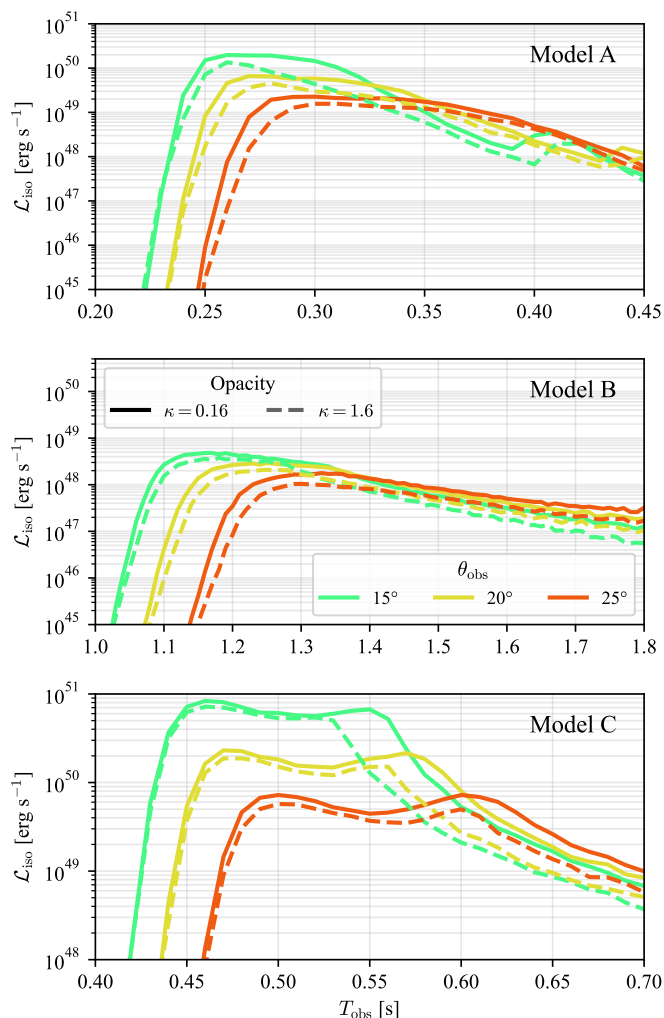


Fig. 9: Same as Fig. 7, now considering two different opacity values:  $\kappa = 0.16 \text{ cm}^2/\text{g}$  (continuous lines) and  $1.6 \text{ cm}^2/\text{g}$  (dotted lines). In this case, we only show three viewing angles, i.e. 15, 20, and 25 degrees, maintaining the same colors employed in Fig. 7.

For each model, we tracked the forward shock in front of the jet-cocoon system up to the photosphere, defined by the condition  $\tau \approx 1/\beta'_{\text{sh}}$ , where  $\beta'_{\text{sh}}$  is the shock velocity in units of  $c$  relative to the unshocked dynamical ejecta. This enabled us to determine self-consistently the onset time of the shock-breakout emission and to compute the corresponding observed GW-EM delay. The calculation explicitly accounts for geometric effects, light-travel-time differences, and relativistic beaming, and was carried out for a range of observer’s viewing angles, adopting a fiducial (frequency independent) opacity of  $\kappa = 0.16 \text{ cm}^2/\text{g}$ .

A key result of our investigation is the remarkably weak dependence of the GW-EM delay on the viewing angle. Between the on-axis view and  $\theta_{\text{obs}} = 30^\circ$ , it varies only by about 20% for models **A** and **C**, and 30% for model **B**. Such a weak dependence makes this time interval a very robust diagnostic to confidently exclude entire classes of jet-launch scenarios, independently of the poorly constrained observer orientation.

Comparing our limited set of models with the observed GW-EM delay of GW170817, we found that our jets are too powerful and/or launched too early. Among the cases explored, model **B** provides the closest match, featuring the most extended interaction between the jet and the surrounding ejecta and yielding a de-

lay in the range  $\approx 1.1 - 1.3 \text{ s}$  for  $\theta_{\text{obs}}$  compatible with GW170817. Nonetheless, the jet is substantially choked and likely inconsistent with other observational signatures (e.g., the jet afterglow signal). These indications will be a reference to start a more systematic exploration of the parameter space, searching for models compatible with GW170817 and, at the same time, investigating in more detail how the different properties of the incipient jet and/or the post-merger environment affect the GW-EM delay.

As a further step, we extended our analysis to the EM emission associated with shock breakout. In particular, we computed the isotropic-equivalent bolometric luminosity resulting from the thermal energy released over time by the shocked material, depending on the viewing angle. In this calculation, we took into account relativistic Doppler shifts, and light-travel-time effects. Since the late-time evolution is followed under the assumption of axisymmetry, we reconstruct the full 3D system in terms of 2D slices through a tomographic procedure. This allows us to take into account non-radial photon propagation from each portion of the whole emitting layer.

To characterize the onset of the emission in a quantitative and model-independent way, we introduced the time  $T_{5\%}$  at which the time-integrated luminosity reaches 5% of the total emitted energy. We found that the corresponding onset times closely track the GW-EM delays obtained from the previous shock-breakout analysis, providing an internal consistency check of our results. As found for the delay, the dependence of  $T_{5\%}$  on the viewing angle is weak, while significant differences arise among the different jet-launch scenarios.

Although the emission mechanism responsible for the observed  $\gamma$ -ray signal of GRB 170817A remains uncertain, we performed a first qualitative comparison between our light curves and the observed prompt emission. Since our luminosity is bolometric, it is expected to exceed that in the reference high-energy band (i.e. 1 keV–10 MeV) by one or two orders of magnitude. The peak luminosity of Model **B** could be reconciled with that of GRB 170817A with a plausible radiative efficiency factor between  $\sim 3 \times 10^{-2}$  and  $10^{-1}$ , whereas the much higher luminosities of Models **A** and **C** appear much more difficult to accommodate.

Another comparison was made in terms of the observed duration of the prompt emission. GRB 170817A is characterized by a  $T_{90}$  of approximately 2 s for the full burst, with a main peak lasting about 0.5 s, as measured in the *Fermi*/GBM energy band. Depending on the model and the viewing angle, the  $T_{90}$  of our bolometric luminosities range from about 0.05 to 0.7 s, with model **B** having the largest durations and thus resulting, also in this case, the closest one to GRB 170817A.

Finally, we computed the shock breakout luminosity with a 10 times larger opacity ( $\kappa = 1.6 \text{ cm}^2/\text{g}$ ). We found that the onset time of the emission is poorly affected ( $< 1.5\%$  difference), implying a very weak dependence of the GW-EM delay on the opacity. This further reinforces the robustness of this observable as a tool to constrain models. Looking at peak luminosity and signal duration, the increased opacity can have non-negligible effects. In particular, depending on the model and the viewing angle, peak luminosities are reduced by at most a factor of 2, while  $T_{90}$  is smaller by no more than 30%.

In future work, in addition to performing a wide parameter exploration, we aim at improving our modelling of the shock-breakout emission, thus enabling more reliable comparisons with the GRB 170817A signal in terms of luminosities and spectra.

## Acknowledgments

The authors acknowledge support from the European Union under NextGenerationEU via the PRIN 2022 Project “EMERGE”, Prot. n. 2022KX2Z3B (CUP C53D23001150006). RC acknowledges further support from the INAF Theory Grant 2023 “AfterJet”, Ob.Fu. 1.05.23.06.02 (CUP C93C23006800005). AP is partially supported by the INAF Mini Grant 2024 “End2End”, Ob.Fu. 1.05.24.07.04 (CUP C93C24008030001). Simulations were performed on the Discoverer (Sofia Tech Park, Bulgaria) and Leonardo (CINECA, Italy) HPC clusters. We acknowledge EuroHPC Joint Undertaking for awarding us access to Discoverer via the Regular Access allocation EHPC-REG-2025R02-007, and CINECA for the availability of high performance computing resources and support on Leonardo through an award under the IS CRA initiative (Grant IsB32 MerJet).

## References

- Abbott, B. P., Abbott, R., Abbott, T. D., et al. 2017a, *ApJ*, 848, L13  
 Abbott, B. P., Abbott, R., Abbott, T. D., et al. 2017b, *Physical Review Letters*, 119, 161101  
 Abbott, B. P., Abbott, R., Abbott, T. D., et al. 2017c, *ApJ*, 848, L12  
 Abramowicz, M. A., Novikov, I. D., & Paczynski, B. 1991, *The Astrophysical Journal*, 369, 175  
 Bauswein, A., Goriely, S., & Janka, H.-T. 2013, *The Astrophysical Journal*, 773, 78  
 Ciolfi, R. 2020, *Monthly Notices of the Royal Astronomical Society: Letters*, 495, L66  
 Dedner, A., Kemm, F., Kröner, D., et al. 2002, *Journal of Computational Physics*, 175, 645  
 Foucart, F. 2023, *Living Reviews in Computational Astrophysics*, 9, 1  
 Geng, J.-J., Zhang, B., Kölligan, A., Kuiper, R., & Huang, Y.-F. 2019, *The Astrophysical Journal*, 877, L40  
 Ghirlanda, G., Salafia, O. S., Paragi, Z., et al. 2019, *Science*, 363, 968  
 Goldstein, A., Veres, P., Burns, E., et al. 2017, *The Astrophysical Journal Letters*, 848, L14  
 Gottlieb, O., Nakar, E., Piran, T., & Hotokezaka, K. 2018, *Monthly Notices of the Royal Astronomical Society*, 479, 588, arXiv: 1710.05896  
 Gupta, S., Sharma, P., & Mignone, A. 2019, arXiv, 000, 1, arXiv: 1906.07200  
 Gupta, S., Sharma, P., & Mignone, A. 2021, *Monthly Notices of the Royal Astronomical Society*, 502, 2733, arXiv: 1906.07200  
 Gutiérrez, E. M., Bhattacharya, M., Radice, D., Murase, K., & Bernuzzi, S. 2025, *Phys. Rev. D*, 111, 063031  
 Hamidani, H. & Ioka, K. 2021, *Monthly Notices of the Royal Astronomical Society*, 500, 627  
 Hotokezaka, K., Kiuchi, K., Kyutoku, K., et al. 2013, *Physical Review D*, 27  
 Kalinani, J. V., Ciolfi, R., Campanelli, M., et al. 2026, *ApJ*, 1000, L35  
 Kasliwal, M. M., Nakar, E., Singer, L. P., et al. 2017, *Science*, 358, 1559  
 Kumar, P. 1999, *The Astrophysical Journal*, 523, L113  
 Martí, J.-M. 2015, *Monthly Notices of the Royal Astronomical Society*, 452, 3106  
 Mattia, G. & Mignone, A. 2021, *Monthly Notices of the Royal Astronomical Society*, 510, 481  
 Metzger, B. D. 2020, *Living Reviews in Relativity*, 23, 1  
 Mignone, A. 2014, *Journal of Computational Physics*, 270, 784  
 Mignone, A., Bodo, G., Massaglia, S., et al. 2007, *The Astrophysical Journal Supplement Series*, 170, 228  
 Mignone, A. & McKinney, J. C. 2007, *Monthly Notices of the Royal Astronomical Society*, 378, 1118  
 Mignone, A., Zanni, C., Tzeferacos, P., et al. 2011, *The Astrophysical Journal Supplement Series*, 198, 7  
 Mooley, K. P., Anderson, J., & Lu, W. 2022, *Nature*, 610, 273, number: 7931  
 Mooley, K. P., Deller, A. T., Gottlieb, O., et al. 2018, *Nature*, 561, 355, 323 citations (Inspire/DOI) [2022-08-21]  
 Nakar, E. 2020, *Physics Reports*, 886, 1  
 Paczyński, B. & Wiita, P. J. 1980, *Astronomy and Astrophysics*, 88, 23, aDS Bibcode: 1980A&A....88..23P  
 Pavan, A., Ciolfi, R., Dreas, E., & Kalinani, J. V. 2025, *Monthly Notices of the Royal Astronomical Society*, 540, 1345  
 Pavan, A., Ciolfi, R., Kalinani, J. V., & Mignone, A. 2021, *Monthly Notices of the Royal Astronomical Society*, 506, 3483  
 Pavan, A., Ciolfi, R., Kalinani, J. V., & Mignone, A. 2023, *Monthly Notices of the Royal Astronomical Society*, 524, 260  
 Radice, D., Perego, A., Hotokezaka, K., et al. 2018, *The Astrophysical Journal Letters*, 869, L35  
 Rybicki, G. B. & Lightman, A. P. 1979, *Radiative processes in astrophysics* (Wiley), publication Title: A Wiley-Interscience Publication ADS Bibcode: 1979rpa..book.....R  
 Toro, E. F. & Titarev, V. A. 2006, *Journal of Computational Physics*, 216, 403  
 Zhang, B.-B., Zhang, B., Sun, H., et al. 2018, *Nature Communications*, 9, 447

## Appendix A: Tilted reference frame

In our 3D simulations, jets are injected along a direction that is orthogonal to the polar axis of the spherical coordinates, i.e. along  $\theta, \phi = \pi/2$ . However, to continue the simulation in 2D under the assumption of axisymmetry, we first need to convert all our data (including vector components) to a spherical coordinate system  $(r, \Theta, \Phi)$  with polar axis aligned with the jet injection axis. Applying the necessary rotation,  $\Theta$  and  $\Phi$  are related to  $\theta$  and  $\phi$  via the following expressions:

$$\begin{aligned} \Theta &= \arccos(\sin \theta \sin \phi) \quad , \\ \Phi &= \pi - \arctan\left(\frac{\cot \theta}{\cos \phi}\right) \quad . \end{aligned} \quad (\text{A.1})$$

For a generic vector in 3D spherical coordinates  $\mathbf{A} = (A_r, A_\theta, A_\phi)$ , the relations are

$$A_\theta = \frac{\cos \phi}{\sin \Theta} A_\Phi \quad , \quad A_\phi = -\frac{\cos \theta \sin \phi}{\sin \Theta} A_\Phi \quad . \quad (\text{A.2})$$

## Appendix B: Reconstruction and evolution of the dynamical ejecta

To properly include the dynamical ejecta in our jet propagation environment, we proceed as follows:

1. We set up a 1D simulation in `PLUTO` starting from the radial profiles along the positive  $z$ -axis of rest-mass density, pressure, and radial velocity imported from the original BNS simulation at  $t = 2$  ms after merger. The front of the dynamical ejecta, at such time, extends up to about 300 km distance.
2. For  $r > 300$  km, we remove the uniform density floor ( $\rho_{\text{floor}} \simeq 6.3 \times 10^4 \text{ g/cm}^3$ ) and corresponding uniform pressure ( $P_{\text{floor}} \simeq 2.79 \times 10^{20} \text{ erg/cm}^3$ ) of the merger simulation, and impose ‘atmospheric’ density and pressure profiles as

$$\rho_{\text{atmo}}(r) = \rho_{\text{floor}} \left(\frac{r}{r_\rho}\right)^{-6.5} \text{ g cm}^{-3}, \quad (\text{B.1})$$

$$P_{\text{atmo}}(r) = P_{\text{floor}} \left(\frac{r}{r_\rho}\right)^{-6.5} \text{ erg cm}^{-3}, \quad (\text{B.2})$$

where  $r_\rho \simeq 73.8$  km (equal to 50 in geometrized units). This gives the red profiles in Figure B.1 (substituting the original blue ones).

3. We evolve the system in 1D for  $\sim 2$  ms, using an inner radius of 25 km (i.e. the portion at  $r < 25$  km is not included in the evolution) and applying a Paczyński–Wiita potential (Paczynski & Wiita 1980) to account for the gravitational pull of the central  $2.596 M_\odot$  black hole.
4. After 2 ms of evolution, we substitute density, pressure, and radial velocity for  $r < 300$  km using the corresponding 1D profiles from the original BNS simulation at the same time. Meanwhile, the material at  $r \geq 300$  km has expanded into the low-density ‘atmosphere’, naturally developing a high velocity tail.
5. We repeat step (4) every 2 ms up to 22 ms after merger, the time over which dynamical ejecta are produced. Note that the ejecta velocity at  $r < 300$  km never exceeds  $0.5 c$  and thus in 2 ms there is no causal connection between the central object and the material at 300 km distance. As a consequence, after any substitution the profiles remain perfectly smooth and

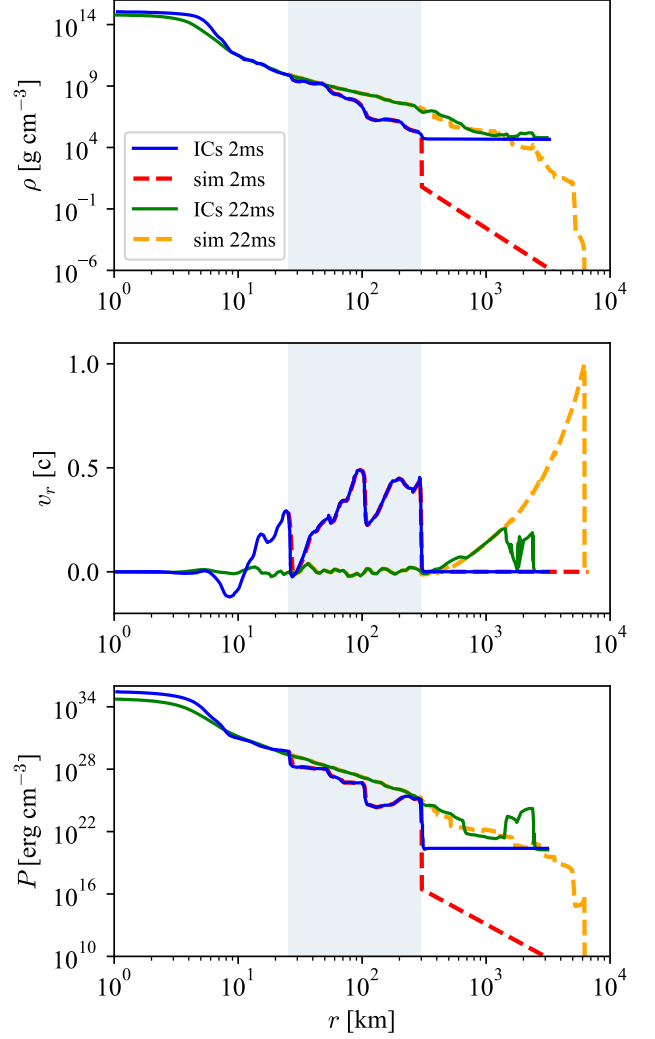


Fig. B.1: Radial profiles of rest-mass density (upper panel), radial velocity (middle panel), and pressure (lower panel). The blue and green lines are the original dynamical ejecta profiles at 2 ms and 22 ms after merger, respectively, while the red and yellow lines are the corresponding profiles reconstructed and simulated in `PLUTO`. The shaded region, from the inner radius of the 1D evolution in `PLUTO` up to 300 km, marks the radial interval where we substitute every 2 ms the evolved profiles with the original ones from the BNS merger simulation (see text for details).

continuous at 300 km. Figure B.1 shows a comparison between the reconstructed dynamical ejecta at 22 ms (yellow) after merger and the equivalent from the original simulation (green). The latter is clearly missing the fast outer part, lost into the high and uniform density floor. The reconstructed profiles are instead similar to those consistently obtained in Kalinani et al. (2026), where BNS merger simulations are performed with very low density floor (in that case, decreasing as  $r^{-6}$ ).

6. We evolve the obtained 1D profiles of density, pressure and radial velocity from 22 ms up to 385 ms after merger. The same profiles, taken either at 185 or at 385 ms after merger, depending on the model under consideration, are then mapped into isotropic distributions in 3D spherical coordinates, to be finally employed to define the dynamical ejecta in our jet

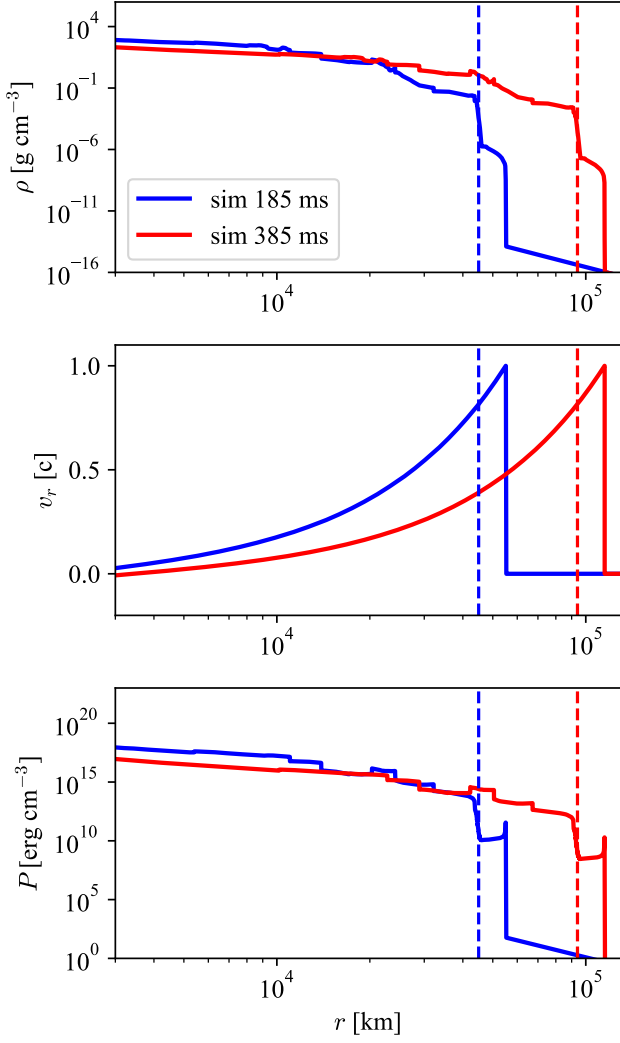


Fig. B.2: Same as Figure B.1 but showing the reconstructed dynamical ejecta at 185 and 385 ms after merger. The dashed vertical lines (at about 45000 and 93000 km, respectively) mark the radii enclosing the bulk of these ejecta, where density drops suddenly by orders of magnitude. The mass outside these radii is negligible ( $\approx 10^{-9} M_{\odot}$ ).

simulations (see Fig. B.2). We note that the total mass of the reconstructed dynamical ejecta is  $0.03 M_{\odot}$ .

## Appendix C: Detailed jet setup and energy calculation

### C.1. Jet luminosity

We start from the stress-energy tensor of a relativistic, unmagnetized fluid

$$T_{\text{HD}}^{\mu\nu} = \rho h c^2 u^{\mu} u^{\nu} + P g^{\mu\nu}, \quad (\text{C.1})$$

where  $u^{\mu} = \Gamma(1, \boldsymbol{\beta})$  is the dimensionless 4-velocity with Lorentz factor  $\Gamma$ ,  $g^{\mu\nu}$  is the metric tensor (which coincides with the Minkowski space-time  $\eta^{\mu\nu}$  in our case),  $h$  is the comoving dimensionless specific enthalpy defined as

$$h = 1 + \frac{\gamma}{\gamma - 1} \frac{P}{\rho c^2}, \quad (\text{C.2})$$

where  $\rho$ ,  $P$ , and  $\gamma$  are the rest-mass density, pressure, and adiabatic index, respectively. Since we use the Taub-Matthews EOS (Mignone & McKinney 2007), pressure and density are linked by

$$\rho h c^2 = \frac{5}{2} P + \sqrt{\rho^2 c^4 + \frac{9}{4} P^2}, \quad (\text{C.3})$$

which gives

$$P = \frac{1}{8} \left( 5h - \sqrt{9h^2 + 16} \right) \rho c^2 \approx \frac{h-1}{4} \rho c^2, \quad (\text{C.4})$$

where the last approximation is valid for hot relativistic jets.

Since our jets are also magnetized, we have to include the electromagnetic contribution to the stress-energy tensor

$$\begin{aligned} T_{\text{EM}}^{\mu\nu} &= F^{\mu\alpha} F^{\nu}_{\alpha} - \frac{1}{4} \eta^{\mu\nu} F_{\alpha\lambda} F^{\alpha\lambda} \\ &= b^2 u^{\mu} u^{\nu} + \frac{b^2}{2} g^{\mu\nu} - b^{\mu} b^{\nu}, \end{aligned} \quad (\text{C.5})$$

where  $b^{\mu} = (b^0, \mathbf{b} \equiv b^i)$  represents the comoving magnetic field,<sup>2</sup> which is related to the lab frame magnetic field  $\mathbf{B}$  via

$$b^0 = \Gamma(\boldsymbol{\beta} \cdot \mathbf{B}), \quad b^i = \frac{B^i}{\Gamma} + \Gamma(\boldsymbol{\beta} \cdot \mathbf{B}) \beta^i, \quad (\text{C.6})$$

and its squared norm is

$$b^2 = \frac{B^2}{\Gamma^2} + (\boldsymbol{\beta} \cdot \mathbf{B})^2 \equiv B^2 - (\boldsymbol{\beta} \times \mathbf{B})^2 \quad (\text{C.7})$$

with  $B^2 = (B^r)^2 + (B^{\theta})^2 + (B^{\phi})^2$ . From (C.7) we can define the comoving magnetization  $\sigma$  as

$$\sigma \equiv \frac{b^2}{\rho h c^2}. \quad (\text{C.8})$$

The total stress-energy tensor for a magnetized fluid is

$$T^{\mu\nu} = \rho h^* c^2 u^{\mu} u^{\nu} + \left( P + \frac{b^2}{2} \right) g^{\mu\nu} - b^{\mu} b^{\nu}, \quad (\text{C.9})$$

where we defined  $h^* \equiv h(1 + \sigma) = h + b^2/\rho c^2$ . Magnetization and pressure can be expressed in terms of  $h^*$  as

$$\sigma = \frac{b^2}{\rho h^* c^2 - b^2}, \quad (\text{C.10})$$

$$P = \frac{h^* - 1}{4} \rho c^2 - \frac{b^2}{4}, \quad (\text{C.11})$$

where we used the ultra-relativistic approximation for the latter formula.

The jet is injected with an axisymmetric structure along the radial direction through a polar cap at the radius  $r_0$  and with half-opening angle  $\theta_j$  and the corresponding one-sided jet luminosity is equal to

$$\begin{aligned} L_j &= 2\pi r_0^2 \int_0^{\theta_j} \left[ \rho_j h_j^* c^2 \Gamma_j^2 \beta_j^r \right. \\ &\quad \left. - B_j^r (\boldsymbol{\beta}_j \cdot \mathbf{B}_j) - \Gamma_j^2 (\boldsymbol{\beta}_j \cdot \mathbf{B}_j)^2 \beta_j^r \right] c \sin \theta d\theta, \end{aligned}$$

<sup>2</sup> We employ a convention where factors  $1/\sqrt{4\pi}$  are included in the magnetic field definition.

$$(C.12) \quad \text{coincides with the radial one } (\Gamma_j \simeq \Gamma_j^r), \text{ implying } \ln(\Gamma_j/\Gamma_j^r) \simeq 0.$$

Thus, we can further simplify our expression for  $\rho(\theta)$  as

$$\rho(\theta) \simeq \rho_0 - \int_0^\theta g(\zeta) d\zeta \quad . \quad (C.18)$$

$\Gamma_j \simeq \Gamma_j^r$  also implies

$$b^\phi \simeq \frac{B^\phi}{\Gamma_j^r} \quad , \quad b^2 \simeq \frac{(B^\phi)^2}{(\Gamma_j^r)^2} + (B^r)^2 \quad , \quad (C.19)$$

and, writing the lab-frame magnetic field components as  $B^\phi = B_0\lambda(\theta)$  and  $B^r = B_0\chi(\theta)$ , the function  $g(\zeta)$  in Eq. (C.18) becomes

$$g(\zeta) = \frac{B_0^2}{(h^* - 1)c^2(\Gamma_j^r)^2} \times \left[ 4\lambda^2(\zeta) \cot \zeta + \frac{\partial[\lambda^2(\zeta) + (\Gamma_j^r)^2\chi^2(\zeta)]}{\partial \zeta} \right] \quad . \quad (C.20)$$

Using the above expression and plugging Eq. (C.18) into Eq. (C.12) leads to the general solution for  $\rho_0$ , which reads

$$\rho_0 = \frac{L_j}{\mathcal{A}_j(\Gamma_j^r)^2 h_j^* \beta_j^r c^3} + \frac{B_0^2 \langle \Lambda(\theta_j) \rangle}{(\Gamma_j^r)^2 c^2 (h_j^* - 1)} + \frac{B_0^2}{h_j^* c^2} \langle \chi^2(\theta_j) \rangle \quad , \quad (C.21)$$

where  $\mathcal{A}_j = 2\pi r_0^2(1 - \cos \theta_j)$ , and we defined

$$\langle \Lambda(\theta_j) \rangle = \frac{1}{1 - \cos \theta_j} \int_0^{\theta_j} \Lambda(\theta) \sin \theta d\theta \quad , \quad (C.22)$$

$$\langle \chi^2(\theta_j) \rangle = \frac{1}{1 - \cos \theta_j} \int_0^{\theta_j} \chi^2(\theta) \sin \theta d\theta \quad , \quad (C.23)$$

with

$$\Lambda(\theta) = \int_0^\theta 4\lambda^2(\zeta) \cot \zeta d\zeta + \lambda^2(\theta) - \lambda^2(0) + (\Gamma_j^r)^2 [\chi^2(\theta) - \chi^2(0)] \quad . \quad (C.24)$$

For the magnetic field functions, we adopt (see Martí 2015; Geng et al. 2019)

$$\lambda(\theta) = \frac{2(\theta/\theta_m)}{1 + (\theta/\theta_m)^2} \quad , \quad (C.25)$$

$$\chi(\theta) = 0.5 \quad , \quad (C.26)$$

with  $\theta_m = 0.4 \theta_j$ .

Since we choose a small angle  $\theta_j = 10^\circ$ , it is possible to approximate the solution to an analytical form with very high precision. To integrate Eqs. (C.24), (C.22), and (C.23), we substitute the trigonometric functions with their Taylor series and obtain

$$\langle \Lambda(\theta_j) \rangle = \int_0^{\theta_j} \frac{\Lambda(\tilde{\theta}) \sin \tilde{\theta}}{1 - \cos \theta_j} d\tilde{\theta} \simeq \frac{3.1\theta_j^2 - 0.419\theta_j^4}{1 - \cos \theta_j} \approx 6.2 \quad , \quad (C.27)$$

where the subscript ‘‘j’’ indicates quantities associated with the jet injection. The (uniform) jet’s angular velocity  $\Omega_{0,j}$  is set by averaging the angular velocity of the surrounding environment, measured at the jet edges. This corresponds to a  $\beta_j^\phi \ll 1$  and thus  $\Gamma_j$  is essentially given by the Lorentz factor along the radial direction.

### C.2. Transverse equilibrium

Transverse equilibrium within the jet, which we impose at the injection radius  $r_0$ , corresponds to the balance between magnetic, thermal, and centrifugal forces acting along the direction of the polar angle  $\theta$ , i.e. orthogonally to the radial and the azimuthal directions (in a spherical coordinate system aligned with the jet injection axis). For a steady flow, this conditions is trivially expressed by  $\nabla_j T^{\theta j} = 0$ . This translates to the following expression (assuming  $\beta^\theta = 0$  and  $B^\theta = 0$ ):

$$\frac{1}{\sqrt{-g}} \partial_\theta (\sqrt{-g} T^{\theta\theta}) + \Gamma^\theta_{\phi\phi} T^{\phi\phi} = 0 \quad , \quad (C.13)$$

where  $\sqrt{-g} = r^2 \sin \theta$  is the determinant of the metric tensor, while  $\Gamma^\theta_{\phi\phi} = -\sin \theta \cos \theta$ . Using the total stress-energy tensor given in Eq. (C.9), we get the following expression for the transverse equilibrium:

$$\frac{\partial}{\partial \theta} \left( P + \frac{b^2}{2} \right) = \cot \theta [(\rho h c^2 + b^2)(\Gamma \beta^\phi)^2 - (b^\phi)^2] \quad . \quad (C.14)$$

Here,  $u^\phi = \Gamma \beta^\phi$  and  $b^\phi$  represent the physically homogeneous azimuthal velocity and magnetic field components, respectively (i.e., the velocity component  $u^i = dX^i/cd\tau$ , with  $X^i = (r, \theta, \phi)$ , multiplied by its corresponding tensor weight  $g_{ii}$ ). From the relation between thermal pressure and density given by Eq. (C.11) we find:

$$\frac{\partial \rho(\theta)}{\partial \theta} - \Gamma^2 (\beta^\phi)^2 \frac{4h^*}{h^* - 1} \cot(\theta) \rho(\theta) = -\frac{1}{(h^* - 1)c^2} \left[ 4 \cot \theta (b^\phi)^2 + \frac{\partial b^2}{\partial \theta} \right] \quad . \quad (C.15)$$

The above first-order linear differential equation for  $\rho(\theta)$  has the form  $\rho'(\theta) - f(\theta)\rho(\theta) = -g(\theta)$ , which admits the following exact solution:

$$\rho(\theta) = e^{\int_0^\theta f(\xi) d\xi} \left[ \rho_0 - \int_0^\theta g(\zeta) e^{-\int_0^\zeta f(\xi) d\xi} d\zeta \right] \quad , \quad (C.16)$$

where  $\rho_0 \equiv \rho(\theta = 0)$ .

Applying the above formula at the jet injection radius  $r_0$ , the exact solution for the integral of  $f(\xi)$  is

$$\int_0^\theta f(\xi) d\xi = \frac{4h^*}{h^* - 1} \int_0^\theta \frac{(\beta_j^\phi)^2 \sin \xi \cos \xi}{1 - (\beta_j^r)^2 - (\beta_j^\phi)^2 \sin^2 \xi} d\xi = \frac{4h^*}{h^* - 1} \ln \left( \frac{\Gamma_j}{\Gamma_j^r} \right) \quad (C.17)$$

where  $\beta_j^\phi = \Omega_{0,j} r_0/c$ . Since  $\beta_j^\phi \ll 1$  and assuming that the jet radial velocity is ultra-relativistic, the total Lorentz factor nearly

and  $\langle \chi^2(\theta_j) \rangle = \chi^2 = 1/4$ .

The solution for  $\rho(\theta)$  in transverse equilibrium reads:

$$\rho(\theta) = \rho_0 - \frac{B_0^2}{(h^* - 1)c^2(\Gamma_j^r)^2} \Lambda(\theta) \quad , \quad (\text{C.28})$$

where

$$\rho_0 = \frac{L_j}{\mathcal{A}_j h_j^* (\Gamma_j^r)^2 \beta_j^r c^3} + \frac{6.2 B_0^2}{(\Gamma_j^r)^2 c^2 (h_j^* - 1)} + \frac{B_0^2}{4 h_j^* c^2} \quad , \quad (\text{C.29})$$

and

$$\Lambda(\theta) \simeq \left[ \frac{8(\theta_m^2 + 3)x^2}{3(x^2 + 1)} - \frac{8}{3}\theta_m^2 \log(1 + x^2) + \lambda^2(\theta) \right] \quad , \quad (\text{C.30})$$

with  $x \equiv \theta/\theta_m$ .

In Figure C.1, we show the angular profiles of various jet injection quantities, referring in particular to our model C. From the comparison between the solution obtained with and without the small angle approximation  $\theta_j \ll 1$ , we see that differences are negligible.

## Appendix D: Shock finder algorithm

We identify and flag cells as shock-zones in our RMHD simulations by imposing the following conditions that a cell should meet at once:

1. converging flow with  $\nabla \cdot \mathbf{v} < 0$  ;
2.  $\nabla T \cdot \nabla \rho > 0$  ;
3. pressure jump between adjacent cells above a given threshold:  $|\nabla P|/|\mathbf{P}_{\min,t} \cdot \Delta \mathbf{x}| \geq \varepsilon_{\text{thresh}}$  .

The temperature is defined in the comoving frame as

$$T = \frac{\mu_{\text{mw}} m_p}{k_B} \frac{P}{\rho} \quad , \quad (\text{D.1})$$

where  $m_p$  is the proton mass,  $\mu_{\text{mw}}$  is the mean molecular weight, and  $k_B$  is the Boltzmann constant. For the latter condition, we consider a rather weak pressure jump threshold of  $\varepsilon_{\text{thresh}} = 10^{-3} - 10^{-2}$ . The quantity  $|\nabla P|/|\mathbf{P}_{\min}$  is a vector with components along each direction given by the ratio between the gradient of pressure in absolute value and the minimum of pressure among adjacent cells, while  $\Delta \mathbf{x}$  is the grid spacing vector (see Mignone et al. 2011).

## Appendix E: Light-curve calculation

### E.1. Shock breakout emission

For each angle and time, we track the shock position with the procedure described in Appendix D. For a fixed angular direction  $\theta_{\text{obs}}$ , we define the shock-breakout time  $t_{\text{bo}}$  as the time at which the shock reaches the radius  $r_{\text{bo}}$  satisfying the condition  $\tau \simeq 1/\beta'_{\text{sh}}$  (see Eq. (4)). After this time, photons trapped within the shock start to be released from the emission radius  $r_e(t)$ , corresponding, at each given time, to the radius where  $\tau \simeq 1/\beta'_{\text{sh}}$ .

Assuming a spherically symmetric system with the same properties we have along  $\theta_{\text{obs}}$ , we compute the comoving-frame thermal energy released in a given simulation timestep  $\Delta t$  between  $t_1$  and  $t_2$  as that contained, at  $t_2$ , between  $r_e(t_2)$  and

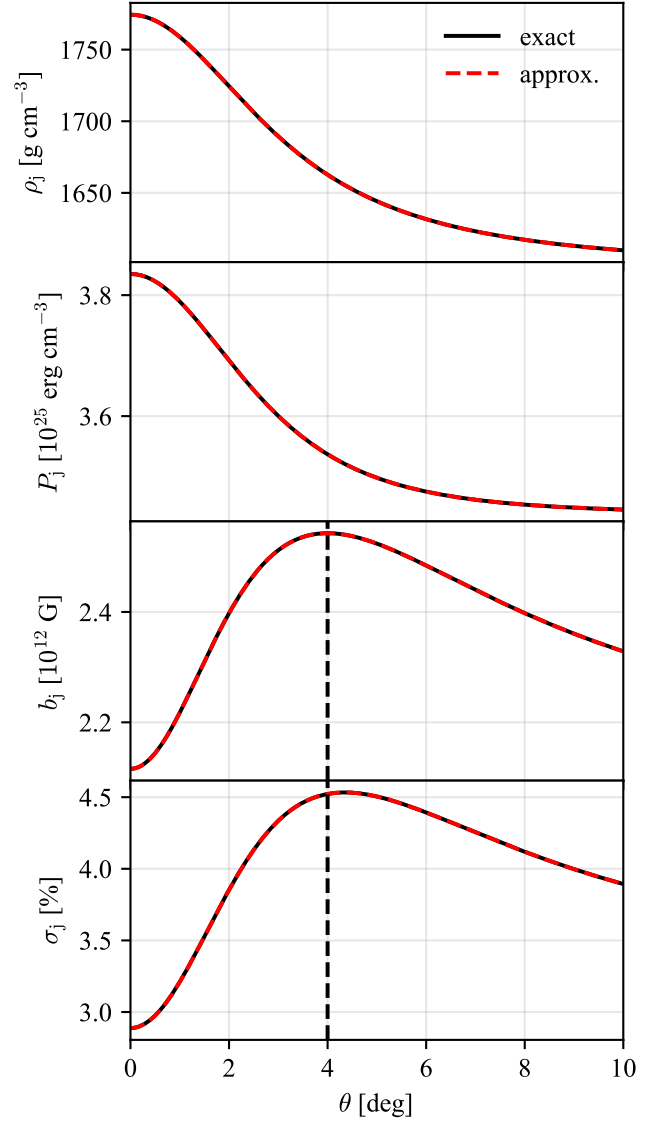


Fig. C.1: Polar angle profiles of jet injection quantities (density, pressure, comoving magnetic field, magnetization) obtained for our model C by imposing transverse equilibrium. The black lines show the direct integration, while the red dashed lines represent our analytical approximation (perfectly matching the exact result). The maximum variation of density and pressure across the angular profile is around 6% and 12%, respectively, resulting in a nearly top-hat configuration. Vertical dashed line marks  $\theta = \theta_m$  (see text).

$r_e(t_1) + v_e(t_1)\Delta t$  (where  $v_e$  is the fluid velocity at the emission radius)

$$\Delta E'(t_1|t_2) \simeq 4\pi \int_{r_e(t_2)}^{r_e(t_1)+v_e(t_1)\Delta t} e'_{\text{th}}(t_2) \Gamma(t_2) r^2 dr \quad , \quad (\text{E.1})$$

where  $e'_{\text{th}} \simeq 3P$  is the comoving thermal energy density. Considering the comoving timestep  $\Delta t' = \Delta t/\Gamma$  (where  $\Gamma$  here is an average value for the emitting layer's Lorentz factor in the given timespan), we can write the comoving energy release per unit time as  $\Delta E'/\Delta t'$ , which represents an average luminosity in the time interval from  $t_1$  and  $t_2$ . We take this quantity as our first estimate of the comoving, isotropic-equivalent bolometric lumi-

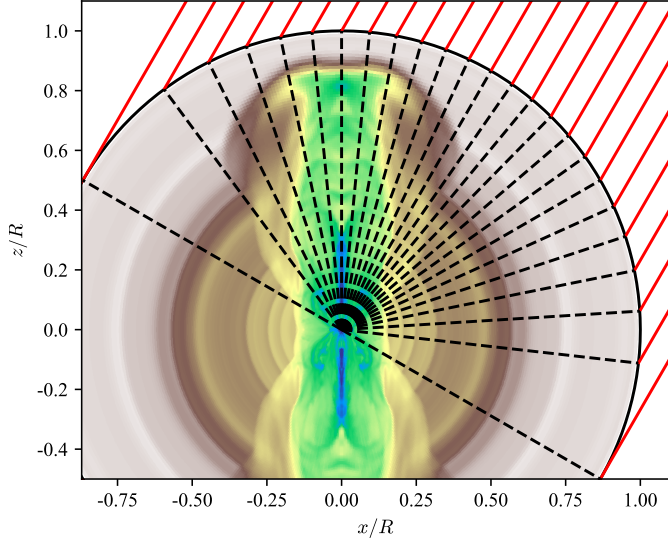


Fig. E.1: 2D section of the total energy density of model **A** at  $t - t_j = 0.6$  s superposed to a pencil of parallel lines connecting to an observer at  $\theta_{\text{obs}} = 30^\circ$  (red lines). The dashed black lines show the corresponding angle at which the rays hit the spherical surface of the dynamical ejecta front, determining their relative inclination. Note that the southern hemisphere is added (copying from the northern one) to cover the full radial extension of the dynamical ejecta front, with radius  $R = 1.9 \times 10^5$  km at that specific moment.

nosity of the shock breakout emission ( $\mathcal{L}'_{\text{iso}}$ ). In the following, we refine this estimate to account for non-radial emission.

## E.2. Including non-radial contributions

Since photon diffusion is not purely radial, the observer will receive radiation from different portions of the emitting layer, with each portion moving along a direction that is in general misaligned with respect to the observing angle. In order to collect radiation from those different portions, we need to account for different light travel times as well as non-radial optical paths.

Being the observer at very large distance compared to the size of the system, the rays connecting the emitting layer with the observer are essentially parallel to each other. Let  $\hat{\mathbf{n}}_{\text{obs}} = (\sin \theta_{\text{obs}}, 0, \cos \theta_{\text{obs}})$  be the unit vector pointing toward an observer at  $\theta = \theta_{\text{obs}}$  (and, for simplicity,  $\phi_{\text{obs}} = 0$ ), and  $\hat{\mathbf{n}} = (\sin \theta \cos \phi, \sin \theta \sin \phi, \cos \theta)$  the normal vector to the spherical surface at given  $(\theta, \phi)$ . The relative angle  $\psi$  between the two unit vectors is given by the following expression:

$$\mu \equiv \cos \psi \equiv \hat{\mathbf{n}}_{\text{obs}} \cdot \hat{\mathbf{n}} = \sin \theta_{\text{obs}} \sin \theta \cos \phi + \cos \theta_{\text{obs}} \cos \theta. \quad (\text{E.2})$$

We first restrict to the meridional plane containing the observer's location. In this case,  $\mu = \cos(\theta - \theta_{\text{obs}})$ . At each evolution time, we consider a pencil of parallel and equally spaced rays oriented towards the observer and covering the full radial extension of the dynamical ejecta front, which is a spherical surface of radius  $R$ , as shown in Figure E.1. While we keep the number of lines fixed to 101 (central one aligned with  $\theta_{\text{obs}}$ , plus  $N = 50$  for each side), the spacing  $\lambda = R/N$  scales according to the dynamical ejecta expansion. The parametric equation describing the pencil of rays is

$$z(x, n) = \frac{1}{\sin \theta_{\text{obs}}} [n\lambda + x \cos \theta_{\text{obs}}] \quad \forall n \in [-N, N], \quad (\text{E.3})$$

where  $n$  is an integer running from  $-N$  to  $N$ . It can be shown that the polar angle  $\theta$  at which a ray shifted by  $n\lambda$  with respect to the line of sight hits the spherical surface of radius  $R$  is

$$\theta_n = \theta_{\text{obs}} - \arcsin\left(\frac{n}{N}\right), \quad (\text{E.4})$$

where positive  $n$  values correspond to rays above the  $n = 0$  line ( $\theta = \theta_{\text{obs}}$ ), while negative  $n$  correspond to rays below the line of sight.

At this point, we extend the above construction to cover also the  $y$  direction: the collection of rays on the  $xz$ -plane (i.e.  $y = 0$ ) becomes a 2D pencil of  $(2N + 1)^2$  rays, where we maintain the same  $N$  and  $\lambda$  also along the  $y$  direction. One specific ray is then identified by the integer  $n$  (see above) and by the new integer  $m \in [-N, N]$ , which corresponds to the plane  $y = m\lambda$ .

Since we evolve assuming axisymmetry, we only have data on the  $y = 0$  plane and need to reconstruct the equivalent information on  $y \neq 0$  planes. This is done by maintaining fixed the  $z$  coordinate and by defining a new  $\hat{x}$  coordinate as

$$\hat{x}(m) = \sqrt{x^2 - (m\lambda)^2}. \quad (\text{E.5})$$

In Figure E.2 we illustrate an example of the resulting 2D slices for  $m = 0, 4, 8, 16$ , referring to model **A** at  $t - t_j = 0.6$  s.

The emitting region, projected on a plane orthogonal to the line of sight, can now be divided into  $(2N + 1)^2$  equal squares centered on each ray of the 2D pencil, identified with the integers  $(m, n)$ . For a given timestep of the evolution  $\Delta t = t_2 - t_1$ , the contribution to the shock-breakout emission coming from one of those  $(2N + 1)^2$  squares will be associated with the comoving-frame thermal energy contained between the emission radius along the specific ray at  $t_2$ , indicated with  $r_e^{m,n}(t_2)$ , and the radius at which the surface  $r_e(t_1, \theta, \phi) + v_e(t_1, \theta, \phi)\Delta t$  intersects this ray, which is approximately given by  $r_e^{m,n}(t_1) + v_e^{m,n}(t_1)\Delta t$ . Naming  $\tilde{x}^{m,n}$  the position along the chosen ray, we call  $\tilde{x}_{\text{in}}^{m,n}$  and  $\tilde{x}_{\text{out}}^{m,n}$  the two positions corresponding to the above radii. The resulting comoving-frame thermal energy can be computed as<sup>3</sup>

$$[\Delta E'(t_1|t_2)]^{m,n} \simeq \lambda(t_2)^2 \int_{\tilde{x}_{\text{in}}^{m,n}}^{\tilde{x}_{\text{out}}^{m,n}} e'_{\text{th}}(t_2) \Gamma_{\perp}(t_2) \Gamma_{\parallel}(t_2) d\tilde{x}^{m,n}, \quad (\text{E.6})$$

where we used the volume transformation  $dV' \equiv dS' d\tilde{x}' = \Gamma_{\perp} dS \Gamma_{\parallel} d\tilde{x} = \Gamma_{\perp} \Gamma_{\parallel} dV$ , with  $\Gamma_{\parallel} = \sqrt{\Gamma^2 \mu^2 + (1 - \mu^2)}$  and  $\Gamma_{\perp} = \sqrt{\mu^2 + \Gamma^2 (1 - \mu^2)}$ .

We note that, in this case, the emission radii are obtained by integrating the optical depth along  $\tilde{x}$ :

$$\tau = \kappa \int \rho(\tilde{x}) \Gamma(\tilde{x}) [1 - \mu\beta(\tilde{x})] d\tilde{x}. \quad (\text{E.7})$$

A criterion analogous to  $\tau \simeq 1/\beta'_{\text{sh}}$  is still adopted, but now considering the motion along the line of sight, i.e.  $\tau \simeq 1/\mu'\beta'_{\text{sh}} = (1 - \mu\beta_{\text{ej}})/[\beta'_{\text{sh}}(\mu - \beta_{\text{ej}})]$ .<sup>4</sup>

<sup>3</sup> Here, we are neglecting the time variation of  $\lambda$  in a timestep  $\Delta t$ , since in our calculations this corresponds to a relative change of order  $10^{-5}$ .

<sup>4</sup> For increasing misalignment with the observer's direction, this expression would eventually diverge as  $\mu$  approaches  $\beta_{\text{ej}}$ . Nonetheless, radiation is already suppressed by relativistic beaming at a smaller misalignment, when  $\mu$  equals the velocity in units of  $c$  of the emitting layer, which is larger than  $\beta_{\text{ej}}$ .

### E.3. Doppler effect and final luminosity

Since the emission layer is moving at relativistic speed (with a certain Lorentz factor  $\Gamma$  and corresponding velocity  $\beta c$ ), the resulting radiation is affected by a relativistic Doppler shift in the direction of the observer that causes the aberration of light, such that the luminosity per unit solid angle  $d\mathcal{L}_{\text{obs}}/d\Omega$  measured by a stationary observer relates to the comoving-frame luminosity per unit solid angle as  $d\mathcal{L}_{\text{obs}}/d\Omega \propto \mathcal{D}^4 d\mathcal{L}'/d\Omega'$  (Rybicki & Lightman 1979), with the Doppler factor  $\mathcal{D}$  given by

$$\mathcal{D} = \frac{dt'}{dT_{\text{obs}}} \equiv \frac{1}{\Gamma(1 - \mu\beta)}, \quad (\text{E.8})$$

where  $t'$  is the proper time in the comoving frame.

Considering Eq. (E.6) and applying the Doppler shift as above, the observed average bolometric luminosity per unit solid angle due to the portion  $(m, n)$  of the emitting layer between the evolution times  $t_1$  and  $t_2$  can be written as

$$\left[ \frac{d\mathcal{L}_{\text{obs}}(t_1|t_2)}{d\Omega} \right]^{m,n} = \mathcal{D}^4 \frac{[\Delta E'(t_1|t_2)]^{m,n}}{4\pi\Delta t'}, \quad (\text{E.9})$$

where  $\Delta t' = \Delta t/\Gamma$ .

The next key element to consider is the arrival time of the emitted photons from the point of view of the observer. Radiation coming from a position  $(r, \theta, \phi)$  at a time  $t$  after merger, will arrive at

$$T_{\text{obs}}(t, r, \theta, \phi) = t - \mu \frac{r}{c}, \quad (\text{E.10})$$

where  $T_{\text{obs}}$  is the time since the observed peak GW signal associated with the BNS merger. Based on this, a contribution to the signal like the one given in Eq. (E.9) will have an average arrival time  $T_k^{m,n}$ , where the index  $k$  indicates the specific evolution timestep under consideration.

Dividing  $T_{\text{obs}}$  in bins of width  $\Delta T$ , we can define a discrete set of times  $T_j$  corresponding to the center of each bin via the running index  $j$ . At this point, we introduce a window function  $\mathcal{W}(T_j - T_k^{m,n})$  that is equal to 1 when  $T_k^{m,n}$  falls within the bin centered in  $T_j$  (i.e.  $|T_j - T_k^{m,n}| < \Delta T/2$ ) and equal to 0 otherwise.

As final step, we reconstruct the full observed bolometric luminosity per unit solid angle as function of the observer time  $T_j$  by summing up the contribution from each portion  $(m, n)$  of the emitting layer and for each timestep:

$$\frac{d\mathcal{L}_{\text{obs}}}{d\Omega}(T_j) = \sum_k \sum_{m,n=-N}^N \left[ \frac{d\mathcal{L}_{\text{obs}}}{d\Omega} \right]_k^{m,n} \mathcal{W}(T_j - T_k^{m,n}). \quad (\text{E.11})$$

Multiplying the above expression by  $4\pi$  gives the isotropic-equivalent bolometric luminosity  $\mathcal{L}_{\text{iso}}(T_j)$ .

We note that, in the above calculation,  $\Delta T$  should be much larger than the evolution timestep  $\Delta t$  and, at the same time, small enough to capture the relevant features of the evolving luminosity. Our choice of  $\Delta T$  satisfies both requirements.

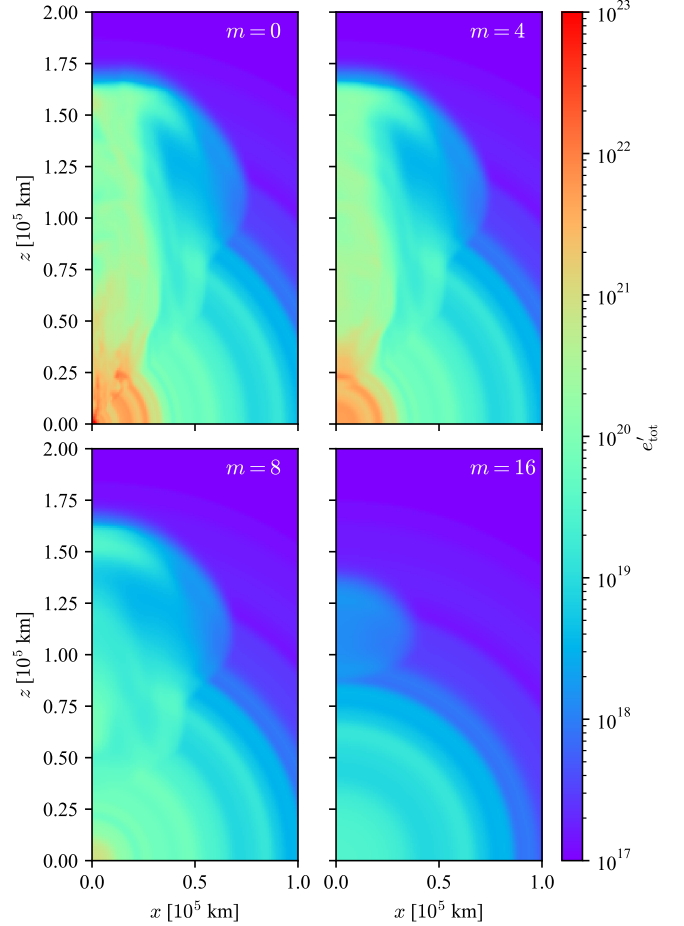


Fig. E.2: Total energy density of model A at  $t - t_j = 0.6$  s, as seen on the planes  $y = m\lambda$ , with  $\lambda = 3.8 \times 10^3$  km and  $m = 0, 4, 8, 16$ .